ON A STRESS RESULTANT GEOMETRICALLY EXACT SHELL MODEL. PART III: COMPUTATIONAL ASPECTS OF THE NONLINEAR THEORY[†]

J.C. SIMO, D.D. FOX and M.S. RIFAI

Division of Applied Mechanics, Department of Mechancial Engineering, Stanford Univeristy, Stanford, CA 94304, U.S.A.

Computational aspects of a geometrically exact stress resultant model presented in Part I of this work are considered in detail. In particular, by exploiting the underlying geometric structure of the model, a configuration update procedure for the director (rotation) field is developed which is singularity free and exact regardless the magnitude of the director (rotation) increment. Our mixed finite element interpolation for the membrane, shear and bending fields presented in Part II of this work are extended to the finite deformation case. The exact linearization of the discrete form of the equilibrium equations is derived in closed form. The formulation is then illustrated by a comprehensive set of numerical experiments which include bifurcation and post-buckling response, we well as comparisons with closed form solutions and experimental results.

1. Introduction

As noted in Part I of this work [1], for nearly twenty years the so-called degenerated solid approach, originally proposed by Ahmad et al. [2] has, to a large extent, dominated computational shell analysis. Subsequent refinements of the basic methodology, particularly within the context of nonlinear analysis, have been proposed by a number of authors; i.e., Ramm [3], Parisch [4], Hughes and Liu [5, 6], Stanley [7], Liu et al. [8], among many others. On the other hand, the classical and modern formulations of shell theories, as in [9–14], have had little impact on the computational literature. In this paper, the third in a sequence, we adopt the latter point of view and consider a geometrically exact shell model formulated entirely in stress resultants. This model, essentially equivalent to a one-director inextensible Cosserat surface, is analyzed in detail in [1, 15]. The understanding of its underlying geometric structure is essential to its numerical implementation. A brief summary of the model along with some results not considered in Part I are given in Section 2.

In this Part, we address in detail the numerical analysis aspects involved in the finite element implementation of the geometrically exact model of Part I. Features of the proposed formulation that we believe are novel include the following:

(i) The weak form of the momentum equations is parametrized in a way that avoids explicit appearance of the Riemannian connection of the mid-surface. In particular, objects such as

Christoffel symbols or the second fundamental form, which are not readily acccessible in a computational context, do not appear explicitly in the formulation.

(ii) We develop a parametrization of the director (rotation) field which is singularity-free and hence optimal for numerical computations. In contrast with the situation encountered in the analysis of geometrically exact rod models, [16–18], this parametrization does not require the use of quaternion parameters to avoid singularities.

(iii) We develop an update procedure for the director (rotation) field which is exact and singularity-free regardless of the magnitude of the incremental rotation. This procedure is obtained by exploiting the geometric structure of the model, and making use of the discrete algorithmic counterpart to the exponential map in the unit sphere S^2 and the connection between SO(3) and S^2. This constitutes one of our main results.

(iv) We extend the mixed finite element treatments of the membrane and bending field, developed in Part II [19] in the context of the linearized theory, to the fully nonlinear range. As in the linearized theory, our results suggest that the present interpolation for the membrane and bending fields, based on a Hellinger–Reissner type of mixed formulation, appears to be optimal within the class of bi-linear elements, even in the fully nonlinear case.

(v) As noted in [20], in nonlinear formulations, linearization and interpolation in general do not commute. In the present context we are able to linearize exactly the discrete weak form of the equilibrium equations to obtain a closed form expression of the discrete tangent operator. This expression is essential in the numerical analysis and simulation of bifurcation problems by continuation methods; see i.e., Keller [21]. In addition, asymptotically quadratic rates of convergence are obtained in iterative Newton-type solution procedures.

The performance of the proposed formulation is assessed numerically through a comprehensive set of examples that include bifurcation and post-buckling response, and comparisons with available (nonlinear) closed form solutions and experimental results. To facilitate and promote comparison with other formulations, we have included in Appendix C a detailed step-by-step description of our implementation.

REMARK about the term 'geometrically exact'. In any numerical solution procedure, there are two different levels of approximation to be considered: the first level concerns the geometry of the shell and the balance equations governing the motion of the shell; the second level is related to the numerical solution of the governing equations. In the present context, the term geometrically exact refers to the first level. Accepting the kinematic assumption which defines the class of admissible motions, the geometry of the shell, as well as the balance equations, are treated exactly. In comparison to other numerical treatments of shell theory, one less level of approximation is made.

2. Summary of the nonlinear theory

For completeness, a brief summary of the nonlinear theory presented in Part I is given. In particular, some new aspects of the theory not considered in Part I but needed for subsequent developments are given in Sections 2.1.2 and 2.2.2.

2.1. Geometry and kinematics of the shell

The nonlinear response of the shell in bending is intimately related to the rotation of the director field. From a geometric point of view, it is convenient to view the rotation of the director field as the motion of a point in the unit sphere S^2; see Fig. 2.1. Furthermore, the unit sphere and the rotation group are related in a manner which is essential to our formulation, in particular to the development of singularity-free parametrizations and configuration update procedures. The basic result needed is not explicitly given in Part I and described in Proposition 2.2.

2.1.1. The rotation group

Following standard notation, we denote by SO(3) the special orthogonal group

$$SO(3) := \{A : \mathbb{R}^3 \to \mathbb{R}^3 \mid A^t = A^{-1} \text{ and } \det A = +1\} . \tag{2.1}$$

Any $A \in SO(3)$ possesses an eigenvector $\psi \in \mathbb{R}^3$ such that $A\psi = \psi$. Geometrically, A represents a finite rotation about ψ. The tangent space to SO(3) at the identity, denoted by $T_1SO(3) := so(3)$, is the set of skew-symmetric tensors defined by

$$so(3) = \{\hat{\Theta} : \mathbb{R}^3 \to \mathbb{R}^3 \mid \hat{\Theta} + \hat{\Theta}^t = 0\} . \tag{2.2}$$

Each $\hat{\Theta} \in so(3)$ possesses an eigenvector $\Theta \in \mathbb{R}^3$ such that $\hat{\Theta}\Theta = 0$. This vector Θ is called the axial vector of $\hat{\Theta}$. One has the isomorphism $\hat{} : so(3) \to \mathbb{R}^3$ defined by the relation

$$\hat{\Theta}h = \Theta \times h \quad \forall h \in \mathbb{R}^3 . \tag{2.3}$$

Finite rotations are elements in SO(3) obtained by exponentiating infinitesimal rotations which are elements of so(3). This mapping, denoted $\exp : so(3) \to SO(3)$, is called the exponential map. One has the explicit expression

$$\exp[\hat{\Theta}] = \cos \|\Theta\| 1 + \frac{\sin \|\Theta\|}{\|\Theta\|} \hat{\Theta} + \frac{1}{\|\Theta\|^2} (1 - \cos \|\Theta\|)\Theta \otimes \Theta , \tag{2.4}$$
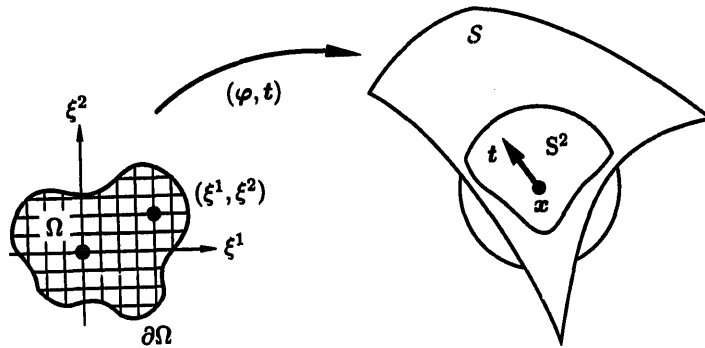

Fig. 2.1. Geometric view of a shell as an inextensible one director Cosserat model. The director corresponds to a point on the unit sphere.

where $\boldsymbol{\Theta}$ is the axial vector of $\hat{\boldsymbol{\Theta}} \in so(3)$. In a (Riemannian) manifold, the exponential mapping maps elements in the tangent space onto elements in the manifold along geodesic curves.

2.1.2. The unit sphere

Geometrically, the inextensibility constraint on the director field of a one-director Cosserat shell model is enforced by introducing the unit sphere defined as

$$S^2 := \{ t \in \mathbb{R}^3 \mid \|t\| = 1 \} . \tag{2.5}$$

In contrast with the rotation group SO(3), the unit sphere S^2 is not a group but simply a differentiable manifold. We think of S^2 as a Riemannian manifold with the standard connection induced by the first fundamental form. The geodesics then, are simply arcs of great circles. The tangent space at $t \in S^2$ is the linear space of vectors tangent to S^2 at t and is defined as

$$T_t S^2 := \{ \Delta t \in \mathbb{R}^3 \mid t \cdot \Delta t = 0 \} . \tag{2.6}$$

As usual, the exponential mapping in S^2 maps tangent vectors $\Delta t \in T_t S^2$ onto points in S^2. In particular, given any point $t \in S^2$ and any tangent $\Delta t \in T_t S^2$ there exists a unique geodesic (i.e., an arc of a great circle) which start as t and is tangent to $\Delta t \in T_t S^2$ at t. This situation is illustrated in Fig. 2.2 and summarized in the following proposition.

PROPOSITION 2.1. The exponential map in $S^2, \exp_t : T_t S^2 \to S^2$, maps the straight line $\varepsilon \mapsto (t, \varepsilon \Delta t) \in T_t S^2$ onto the unique great circle (geodesic) passing through $t \in S^2$ and tangent to $\Delta t \in T_t S^2$, according to

$$t_\varepsilon := \exp_t [\varepsilon \Delta t] = \cos (\varepsilon \|\Delta t\|) t + \frac{\sin (\varepsilon \|\Delta t\|)}{\|\Delta t\|} \Delta t \quad \forall \varepsilon \in \mathbb{R} . \tag{2.7}$$

PROOF. The first part is a standard result in differential geometry; see, i.e., [22, p. 79]. To check (2.7) simply note that t_ε is in the plane spanned by $\{t, n\}$, where $n := \Delta t / \|\Delta t\| \in S^2$; see
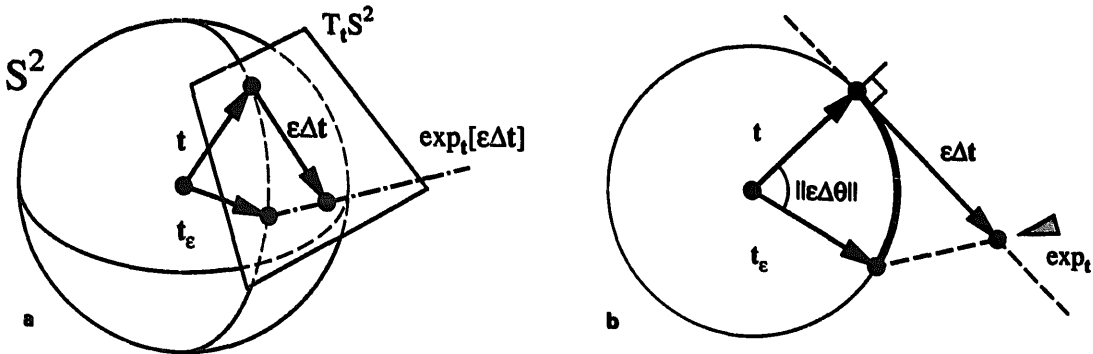

Fig. 2.2.(a) The unique geodesic starting at $t \in S^2$ and tangent to $\Delta t \in T_t S^2$. This curve (an arc of great circle) is the image of the straight line $t + \varepsilon \Delta t$. (b) Illustration of (2.7) for the exponential map.

Fig. 2.2(b). Since the length of the arc between t and t_ε is precisely $\varepsilon\|\Delta t\|$, it follows that $t \cdot t_\varepsilon = \cos(\varepsilon\|\Delta t\|)$ and $n \cdot t_\varepsilon = \sin(\varepsilon\|\Delta t\|)$. $\Box$

2.1.3. Relation between S^2 and SO(3)

The rotation group, SO(3), and the unit sphere, S^2, are connected through the following relation which is fundamental to our development of the theory, its numerical parametrization and implementation. This result is given in Proposition 2.2 and illustrated in Fig. 2.3.

PROPOSITION 2.2. Let $t \in S^2$ be given. By Proposition 2.1, any $\Delta t \in T_t S^2$ defines a point $\bar{t} := \exp_t[\Delta t] \in S^2$ located on the geodesic starting at t and tangent to Δt. Then there is a unique rotation $\Delta\Lambda \in$ SO(3) which rotates t onto $\bar{t}$,

$$\bar{t} := \exp_t[\Delta t] = \Delta\Lambda t, \tag{2.8}$$

whose rotation axis is parallel to $t \times \Delta t$ and is given by

$$\Delta\Lambda = \cos\|\Delta t\|\mathbf{1} + \frac{\sin\|\Delta t\|}{\|\Delta t\|}[\widehat{t \times \Delta t}] + \frac{(1-\cos\|\Delta t\|)}{\|\Delta t\|^2}(t \times \Delta t) \otimes (t \times \Delta t). \tag{2.9}$$

PROOF. $t, \bar{t} \in S^2$ and $\Delta t \in T_t S^2$ are all in a plane normal to $t \times \Delta t$. Since $\|t\| = \|\bar{t}\| = 1$, it follows that $t \times \Delta t$ defines the axis of rotation of an orthogonal transformation that maps t onto $\bar{t}$. Furthermore, since $\Delta t \cdot t = 0$, from (2.7) we have

$$\bar{t} \cdot t = \cos(\|\Delta t\| \quad \Rightarrow \quad \|\Delta t\| = \text{angle}(t, \bar{t}). \tag{2.10a}$$

Finally, making again use of condition $t \cdot \Delta t = 0$ along with standard vector product identities, we easily conclude that

$$\|t \times \Delta t\|^2 = t \cdot (\Delta t \times (t \times \Delta t)) = \|\Delta t\|^2. \tag{2.10b}$$

Thus, $\|t \times \Delta t\| = \|\Delta t\|$. Result (2.9) then follows from (2.4) by setting $\Theta = t \times \Delta t$. $\Box$

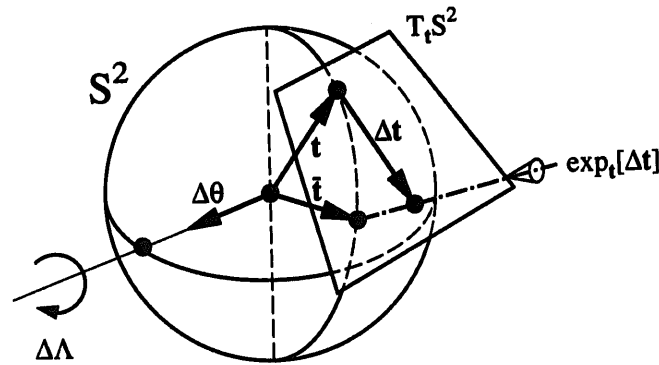Fig. 2.3. Given $\Delta t \in T_t S^2$, the point $\bar{t} = \exp_t[\Delta t] \in S^2$ is obtained through the singularity-free rotation $\Delta\Lambda \in$ SO(3) given by (2.9).

REMARK 2.1. Expressions (2.7) and (2.9) for the exponential map in S^2 and the associated rotation $\Delta\Lambda$ are singularity-free in the sense that they are always well-conditioned for any magnitude of $\Delta t \in T_t S^2$.

2.1.4. Kinematic description of the shell

We introduce the generalized Kirchhoff hypothesis, along with the classical assumption of inextensibility of the director field as follows. The mid-surface of the shell is defined by the mapping $\varphi : \bar{\mathscr{A}} \to \mathbb{R}^3$, whereas the mapping $t : \bar{\mathscr{A}} \to S^2$ defines the director field. Let $\mathscr{C}$ be the manifold of mappings

$$\mathscr{C} := \{\Phi := (\varphi, t) \mid \bar{\mathscr{A}} \subset \mathbb{R}^2 \to \mathbb{R}^3 \times S^2\} . \tag{2.11}$$

Here, $\bar{\mathscr{A}} \subset \mathbb{R}^2$ is compact, with smooth bundary $\partial\mathscr{A}$, and points denoted by $(\xi^1, \xi^2) \in \bar{\mathscr{A}}$. We denote by $\partial_\varphi \mathscr{A} \subset \partial\mathscr{A}$ and $\partial_t \mathscr{A} \subset \partial\mathscr{A}$ the parts of $\partial\mathscr{A}$ where φ and t are prescribed. With the preceding notation and according to the generalized Kirchhoff hypothesis, any placement of the shell in $\mathbb{R}^3$ is assumed to be defined as the set

$$\mathscr{S} := \{x \in \mathbb{R}^3 \mid x = \varphi + \xi t, \text{ where } (\varphi, t) \in \mathscr{C} \text{ and } \xi \in [h^-, h^+]\} , \tag{2.12}$$

where $h = h^+ - h^-$ is the thickness of the shell. Consequently, since any $\Phi := (\varphi, t)$ in $\mathscr{C}$ uniquely defines a placement $\mathscr{S}$ of the shell-like body in $\mathbb{R}^3$, one refers to $\mathscr{C}$ as the abstract configuration space. $\mathscr{C}$ is a differentiable manifold with tangent space at $\Phi \in \mathscr{C}$ denoted by $T_\Phi \mathscr{C}$ and defined below. We denote by $\mathscr{S}^0$ the reference placement of the shell, and append the superscript '0' to geometric objects associated with $\mathscr{S}^0$. Further, we let $d\mu = \bar{j} \, d\xi^1 \, d\xi^2$ and $d\mu^0 = \bar{j}^0 \, d\xi^1 \, d\xi^2$ be the mid-surface measures in the current and reference configurations, respectively, where

$$\bar{j} := (\varphi_{,1} \times \varphi_{,2}) \cdot t , \qquad \bar{j}^0 := (\varphi^0_{,1} \times \varphi^0_{,2}) \cdot t^0 , \qquad \bar{J} := \bar{j}/\bar{j}^0 . \tag{2.13}$$

We refer to $\{\varphi_{,\alpha}, t\} \equiv \{a_\alpha, a_3\}$ and $\{\varphi^0_{,\alpha}, t^0\} \equiv \{a^0_\alpha, a^0_3\}$ as the surface convected frame in the current placement $\mathscr{S}$ and reference placement $\mathscr{S}^0$ of the shell, respectively; see Fig. 2.4. Further, we denote by $\{e_1, e_2, e_3\}$ the fixed inertial frame in Euclidean space, and choose $e_i = \delta^I_i E_I$, where $\{E_I\}$ is the standard basis in $\mathbb{R}^3$. We then have the component expressions

$$\varphi = \varphi^i e_i , \qquad \varphi_{,\alpha} = \varphi^i_{,\alpha} e_i , \qquad \delta\varphi = \delta\varphi^i e_i ,$$
$$t = t^i e_i , \qquad \delta t = \delta t^i e_i , \qquad \Lambda = \Lambda^i_I e_i \otimes E^I . \tag{2.14}$$

The relative deformation gradient (for $\xi = 0$) at $x^0 = \varphi^0(\xi^1, \xi^2)$ is a linear map $\bar{F} : T_{x^0}\mathscr{S}^0 \to T_x\mathscr{S}$ mapping vector fields defined on the reference mid-surface onto vector fields defined on the current mid-surface, and given by

$$\bar{F} := a_\alpha \otimes a^{0\alpha} + t \otimes a^{03} \equiv a_i \otimes a^{0i} . \tag{2.15}$$
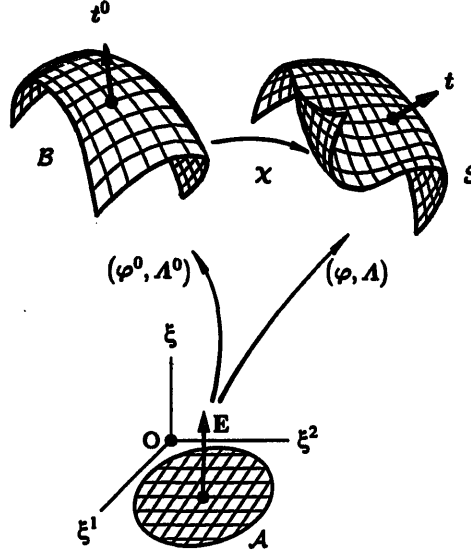
As in Part I, we set

Fig. 2.4. Basic kinematic quantities associated with the reference and current placements of the shell, $\mathscr{S}^0 \equiv B$ and $\mathscr{S}$, respectively.

$$a_{\alpha\beta} = \varphi_{,\alpha} \cdot \varphi_{,\beta} , \qquad \gamma_\alpha = \varphi_{,\alpha} \cdot t , \qquad \kappa_{\alpha\beta} = \varphi_{,\alpha} \cdot t_{,\beta} , \qquad (2.16)$$

and use identical definitions for the reference placement $\mathscr{S}^0$, so that the unit tensor relative to $\mathscr{S}^0$, denoted by $\mathbf{1}^0 := a_i^0 \otimes a^{0^i}$, takes the form

$$\mathbf{1}^0 = a_{\alpha\beta}^0 a^{0\alpha} \otimes a^{0\beta} + \gamma_\alpha^0 (a^{0\alpha} \otimes a^{0^3} + a^{0^3} \otimes a^{0\alpha}) + a^{0^3} \otimes a^{0^3} . \qquad (2.17)$$

Therefore, with $\bar{E} := \frac{1}{2}[\bar{F}^t\bar{F} - \mathbf{1}^0]$, the Lagrangian strain tensor relative to the reference surface, becomes

$$\bar{E} = \frac{1}{2}(a_{\alpha\beta} - a_{\alpha\beta}^0)a^{0\alpha} \otimes a^{0\beta} + \frac{1}{2}(\gamma_\alpha - \gamma_\alpha^0)(a^{0\alpha} \otimes a^{0^3} + a^{0^3} \otimes a^{0\alpha}) . \qquad (2.18)$$

2.2. The variational form of the momentum balance equations

In what follows, attention is restricted to the static case. The weak form of the equilibrium equations, then, is obtained merely by dropping the inertia terms in the general expression derived in Part I.

2.2.1. Admissible variations. Linearization

Let $\Phi \in \mathscr{C}$ be a configuration, and let $\varepsilon \mapsto \Phi_\varepsilon \in \mathscr{C}$ be a curve of configurations starting at Φ; that is, $\Phi_\varepsilon|_{\varepsilon=0} = \Phi$. By definition, the tangent field to one such curve at $\varepsilon = 0$ is called an admissible variation; we use the notation $\delta\Phi = [d/d\varepsilon]_{\varepsilon=0}\Phi_\varepsilon$. The space of admissible variations at Φ is the tangent space to $\mathscr{C}$ at Φ and is denoted by $T_\Phi \mathscr{C}$. By linearizing configurations in (2.11), it follows that $T_\Phi \mathscr{C}$ is given by

$$T_\Phi \mathscr{C} = \{ \Phi := (\delta\varphi, \delta t) : \bar{\mathscr{A}} \to \mathbb{R}^3 \times T_t S^2 \mid \delta\varphi|_{\partial_\varphi \mathscr{A}} = 0 \text{ and } \delta t|_{\partial_t \mathscr{A}} = 0 \} . \qquad (2.19)$$

In the development that follows, one is often confronted with the linearization of quantities at a given configuration $\Phi := (\varphi, t) \in \mathscr{C}$ in the direction of an admissible variable $\Delta\Phi = (\Delta\varphi, \Delta t) \in T_\Phi\mathscr{C}$. This is the case, for instance, in the linearization of the weak form of the momentum balance equations. A systematic linearization procedure is outlined below.

Let $H : \mathscr{C} \rightarrow \mathbb{R}^m$ be a real vector-valued function on $\mathscr{C}$. By definition, the linearization of H at $\Phi \in \mathscr{C}$ in the direction $\Delta\Phi \in T_\Phi\mathscr{C}$, denoted by $DH(\Phi) \cdot \Delta\Phi$, is given by

$$DH(\Phi) \cdot \Delta\Phi := \frac{d}{d\varepsilon}\Big|_{\varepsilon=0} H(\Phi_\varepsilon) , \qquad (2.20)$$

where Φ_ε denotes a one-parameter curve of configurations $\varepsilon \mapsto \Phi_\varepsilon = (\varphi_\varepsilon, t_\varepsilon) \in \mathscr{C}$ with the property that

$$\Phi_\varepsilon\big|_{\varepsilon=0} = (\varphi, t) := \Phi \in \mathscr{C} \qquad (2.21a)$$

and

$$D\Phi \cdot \Delta\Phi := \frac{d}{d\varepsilon}\Big|_{\varepsilon=0} \Phi_\varepsilon = (\Delta\varphi, \Delta t) \in T_\Phi\mathscr{C} . \qquad (2.21b)$$

Thus, given such a one-parameter family of configurations, the calculation of (2.20) reduces to ordinary differentiation with respect to $\varepsilon > 0$. Owing to the linear nature of $\mathbb{R}^3$, the one-parameter curve φ_ε is constructed simply as

$$\varphi_\varepsilon = \varphi + \varepsilon\Delta\varphi . \qquad (2.22)$$

However, since S^2 is not a linear space but a differential manifold, the one-parameter curve t_ε is constructed by means of the exponential map in S^2. According to (2.8) or (2.9), we set

$$t_\varepsilon = \Delta\Lambda_\varepsilon t := \exp[\varepsilon\widehat{\Delta\theta}]t = \exp_t[\varepsilon\Delta t] , \qquad (2.23)$$

where $\Delta t := \widehat{\Delta\theta}t = \Delta\theta \times t$ is in $T_t S^2$. It then follows that

$$t_\varepsilon\big|_{\varepsilon=0} = t \qquad (2.24a)$$

and

$$\frac{d}{d\varepsilon}\Big|_{\varepsilon=0} t_\varepsilon := \Delta t = \widehat{\Delta\theta}t = \Delta\theta \times t . \qquad (2.24b)$$

Therefore, the curve $\varepsilon \mapsto (\varphi_\varepsilon, t_\varepsilon) \in \mathscr{C}$ defined by (2.22) and (2.23) satisfies the required properties (2.21a,b). One should carefully note that in expressions of the form $\Delta t := \Delta\theta \times t$, $\widehat{\Delta\theta} \in so(3)$ and not $\Delta t \in T_t S^2$ is the primitive independent variable which is held constant in the linearization process. (Thus for any $\delta\Phi \in T_\Phi\mathscr{C}$, this implies that $D\Delta\theta \cdot \delta\Phi = 0$, while $D\Delta t \cdot \delta\Phi \neq 0$.)

2.2.2. Stress resultants

As in Part I, we denote by $\tilde{n}^{\alpha\beta}$ and $\tilde{q}^\alpha$ the components of the effective stress resultants and by $\tilde{m}^{\alpha\beta}$ the components of the director couple resultant relative to $\{\varphi_\alpha, t\}$; that is

$$\tilde{n} = \tilde{n}^{\alpha\beta}a_\alpha \otimes a_\beta , \qquad \tilde{q} = \tilde{q}^\alpha a_\alpha , \qquad \tilde{m} = \tilde{m}^{\alpha\beta}a_\alpha \otimes a_\beta . \qquad (2.25)$$

We recall that an important consequence of balance of angular momentum is the symmetry of the in-plane effective stress resultant components;

$$\tilde{n} = \tilde{n}^t, \quad \text{i.e., } \tilde{n}^{\alpha\beta} = \tilde{n}^{\beta\alpha} \quad \text{for } \alpha, \beta \in \{1, 2\}. \tag{2.26}$$

We introduce stress resultants and stress couples relative to the reference state via pull-back with $\bar{F}$; that is, we define

$$\tilde{N} := J\bar{F}^{-1}\tilde{n}\bar{F}^{-t}, \qquad \tilde{M} := J\bar{F}^{-1}\tilde{m}\bar{F}^{-t}, \qquad \tilde{Q} := J\bar{F}^{-1}\tilde{q}. \tag{2.27}$$

Since $a_\alpha = \bar{F}a_\alpha^0$, it follows from (2.25) and (2.27) that the components of $\tilde{n}$, $\tilde{q}$ and $\tilde{m}$ relative to the basis $\{a_\alpha, a_3\}$ are equal (up to a factor of J) to the components of $\tilde{N}$, $\tilde{Q}$ and $\tilde{M}$ relative to $\{a_\alpha^0, a_3^0\}$; i.e.,

$$\tilde{N} = J\tilde{n}^{\alpha\beta}a_\alpha^0 \otimes a_\beta^0, \qquad \tilde{Q} = J\tilde{q}^\alpha a_\alpha^0, \qquad \tilde{M} = J\tilde{m}^{\alpha\beta}a_\alpha^0 \otimes a_\beta^0. \tag{2.28}$$

2.2.3. Matrix notation

For convenience, we arrange the stress resu~ants and stress couple components as column matrices, as indicated in Box 1. Likewise, the (nonlinear) membrane, shearing and bending Lagrangian strain measures are given in matrix notation as

$$\varepsilon(\Phi) = \frac{1}{2}\begin{bmatrix} a_{11} - a_{11}^0 \\ a_{22} - a_{22}^0 \\ 2(a_{12} - a_{12}^0) \end{bmatrix}, \qquad \delta(\Phi) = \begin{bmatrix} \gamma_1 - \gamma_1^0 \\ \gamma_2 - \gamma_2^0 \end{bmatrix}, \qquad \rho(\Phi) = \begin{bmatrix} \kappa_{11} - \kappa_{11}^0 \\ \kappa_{22} - \kappa_{22}^0 \\ 2(\kappa_{12} - \kappa_{12}^0) \end{bmatrix}. \tag{2.29}$$

In addition, we set

$$\tilde{r}^t := [\tilde{n}^{11} \ \tilde{n}^{22} \ \tilde{n}^{12} \ \tilde{q}^1 \ \tilde{q}^2 \ \tilde{m}^{11} \ \tilde{m}^{22} \ \tilde{m}^{(12)}]^t. \tag{2.30}$$

Further, in what follows, $\tilde{n}$, $\tilde{q}$ and $\tilde{m}$ will always refer to the matrix expressions in Box 1 unless otherwise explicitly indicated. We assume that

$$\mathcal{V}_r := \{\tilde{r} = (\tilde{n}, \tilde{q}, \tilde{m}) \mid \tilde{r} \in [L_2(\mathcal{A})]^8\}. \tag{2.31}$$

Finally, $G_{\text{ext}}(\delta\Phi): T_\Phi\mathcal{C} \to \mathbb{R}$ is the virtual work of the external loading given by

$$G_{\text{ext}}(\delta\Phi) = \int_{\mathcal{A}} [\bar{n} \cdot \delta\varphi + \bar{m} \cdot \delta t] \, d\mu^0 + \int_{\partial_n\mathcal{A}} \bar{\bar{n}} \cdot \delta\varphi \bar{j} \, ds + \int_{\partial_m\mathcal{A}} \bar{\bar{m}} \cdot \delta t \, \bar{j} \, ds. \tag{2.32}$$

Here, $\bar{\bar{n}}$ and $\bar{\bar{m}}$ are the prescribed resultant force and the prescribed director couple on the boundary $\partial_n\mathcal{A}$ and $\partial_m\mathcal{A}$, respectively, where $\partial_n\mathcal{A} \cap \partial_\varphi\mathcal{A} = \emptyset$ and $\partial_m\mathcal{A} \cap \partial_t\mathcal{A} = \emptyset$.

REMARK 2.2. (Enforcement of the inextensibility constraint.) The constraint condition $\|t\| = 1$ on the director field determines the linearized constraint $t \cdot \delta t = 0$ on the director

Box 1
Weak form. Matrix expressions

— Mid-surface variation, effective stress resultant and stress couple vectors:

$$\delta\varphi = \begin{bmatrix} \delta\varphi^1 \\ \delta\varphi^2 \\ \delta\varphi^3 \end{bmatrix}; \quad \tilde{n} = \bar{J}\begin{bmatrix} \tilde{n}_{11} \\ \tilde{n}_{22} \\ \tilde{n}^{(12)} \end{bmatrix}, \quad \tilde{q} = \bar{J}\begin{bmatrix} \tilde{q}^1 \\ \tilde{q}^2 \end{bmatrix}, \quad \tilde{m} = \bar{J}\begin{bmatrix} \tilde{m}^{11} \\ \tilde{m}22 \\ \tilde{m}^{(12)} \end{bmatrix}, \quad \tilde{r} = \begin{bmatrix} \tilde{n} \\ \tilde{q} \\ \tilde{m} \end{bmatrix}.$$

— Director variations, inextensibility constraint 5 DOF [$\delta t \cdot t = \delta T \cdot E = 0$]:

$$\delta t = \begin{bmatrix} \delta t^1 \\ \delta t^2 \\ \delta t^3 \end{bmatrix}, \quad \delta T = \begin{bmatrix} \delta T^1 \\ \delta T^2 \end{bmatrix}, \quad \delta t = \bar{A}\delta T \quad \text{and} \quad \bar{A} := \begin{bmatrix} A_{11} & A_{12} \\ A_{21} & A_{22} \\ A_{31} & A_{32} \end{bmatrix}.$$

— Matrix differential operators:

$$\mathbb{B}_m = \begin{bmatrix} \varphi^t_{,1}\dfrac{\partial}{\partial\xi^1} \\ \varphi^t_{,2}\dfrac{\partial}{\partial\xi^2} \\ \varphi^t_{,1}\dfrac{\partial}{\partial\xi^2} + \varphi^t_{,2}\dfrac{\partial}{\partial\xi^1} \end{bmatrix}_{3\times3}, \quad \mathbb{B}_{bm} = \begin{bmatrix} t^t_{,1}\dfrac{\partial}{\partial\xi^1} \\ t^t_{,2}\dfrac{\partial}{\partial\xi^2} \\ t^t_{,1}\dfrac{\partial}{\partial\xi^2} + t^t_{,2}\dfrac{\partial}{\partial\xi^1} \end{bmatrix}_{3\times3},$$

$$\mathbb{B}_{sm} = \begin{bmatrix} t^t\dfrac{\partial}{\partial\xi^1} \\ t^t\dfrac{\partial}{\partial\xi^2} \end{bmatrix}_{2\times3}, \quad \mathbb{B}_{sb}\begin{bmatrix} \varphi^t_{,1} \\ \varphi^t_{,2} \end{bmatrix}_{2\times3}\bar{A}_{3\times2}, \quad \mathbb{B}_{bb} = \mathbb{B}_m\bar{A}_{3\times2}.$$

— Weak form $G(\tilde{r}, \Phi; \delta\Phi): \mathcal{V}_r \times \mathcal{C} \times T_\Phi\mathcal{C} \rightarrow \mathbb{R}$:

$$G(\tilde{r}, \Phi; \delta\Phi) := \int_{\mathcal{A}} \{[\mathbb{B}_m\delta\varphi]^t\tilde{n} + [\mathbb{B}_{sm}\delta\varphi + \mathbb{B}_{sb}\delta T]^t\tilde{q} + [\mathbb{B}_{bm}\delta\varphi + \mathbb{B}_{bb}\delta T]^t\tilde{m}\} \, d\mu^0 - G_{ext}(\delta\Phi).$$

admissible variations. Therefore, director variations δt only have two independent components. This results in a five degree-of-freedom formulation.

The linearized constraint condition $\delta t \cdot t = 0$ can be identically satisfied by introducing an orthogonal transformation Λ such that $E \mapsto t = \Lambda E \in S^2$, so that $\delta t = \Lambda\delta T$, where $E \in S^2$ is a fixed vector relative to the inertial frame. This orthogonal transformation is uniquely constructed incrementally during the solution procedure by making use of Proposition 2.2, as explained in detail in Section 4. Observe that since $t \cdot \delta t = \Lambda E \cdot \Lambda\delta T = E \cdot \delta T = 0$, by choosing E coincident with one of the inertial basis vectors; say $E = E_3$, it follows that δT admits the representation $\delta T = \delta T^1 E_1 + \delta T^2 E_2$. Thus, we effectively obtain the five-degree-of-freedom formulation summarized in Box 1.

2.3. Constitutive equations; mixed variational formulation

Following the developments in Part II, we shall consider a variational formulation of the following form:

  i. A Hellinger–Reissner formulation for the membrane and bending fields.
  ii. A Hu–Washizu variational formulation for the transverse shear field.

In order to place the simple, properly invariant, constitutive model proposed in Part I in the mixed variational setting, we consider the functional $\Pi : \mathcal{V}_r \times [L(\mathcal{A})]^2 \times \mathcal{C} \to \mathbb{R}$ of the form

$$\Pi(\tilde{r}, \bar{\delta}, \Phi) = \Pi_m(\Phi, \tilde{n}) + \Pi_b(\Phi, \tilde{m}) + \Pi_s(\Phi, \bar{\delta}, \tilde{q}) + \Pi_{ext}(\Phi) . \tag{2.33}$$

Here, $\Pi_{ext} : \mathcal{C} \to \mathbb{R}$ is the potential energy of the external loading, such that

$$D\Pi_{ext}(\Phi) \cdot \delta\Phi = -G_{ext}(\delta\Phi) \tag{2.34}$$

for any $\delta\Phi \in T_\Phi \mathcal{C}$, where $G_{ext} : T_\Phi \mathcal{C} \to \mathbb{R}$ is defined by (2.32). In addition, $\tilde{r} := (\tilde{n}, \tilde{q}, \tilde{m}) \in \mathcal{V}_r$ and

$$\Pi_m(\Phi, \tilde{n}) := \int_{\mathcal{A}} \tilde{n}^t[-\tfrac{1}{2}\mathbb{C}_m^{-1}\tilde{n} + \varepsilon(\Phi)] \, d\mu^0 ,$$

$$\Pi_b(\Phi, \tilde{m}) := \int_{\mathcal{A}} \tilde{m}^t[-\tfrac{1}{2}\mathbb{C}_b^{-1}\tilde{m} + \rho(\Phi)] \, d\mu^0 , \tag{2.35}$$

$$\Pi_s(\Phi, \bar{\delta}, \tilde{q}) := \int_{\mathcal{A}} [\tfrac{1}{2}\bar{\delta}^t\mathbb{C}_s\bar{\delta} + \tilde{q}^t[\delta(\Phi) - \bar{\delta}]] \, d\mu^0 .$$

We assume that $\tilde{n} \in [L_2(\mathcal{A})]^6$, $\tilde{m} \in [L_2(\mathcal{A})]^6$ and $\bar{\delta} \in [L_2(\mathcal{A})]^2$. Further, observe that

$$D\Pi \cdot \delta\Phi \equiv \frac{d}{d\varepsilon}\bigg|_{\varepsilon=0} \Pi(\tilde{r}, \bar{\delta}, \Phi_\varepsilon) \equiv G(\tilde{r}, \Phi; \delta\Phi) \tag{2.36}$$

for all $\delta\Phi \in T_\Phi \mathcal{C}$, where $G(\tilde{r}, \Phi; \delta\Phi) = 0$ is the weak form of the equilibrium equations given in Box 1. Finally, we assume the simple constitutive model

$$\mathbb{C}_m^{-1} := \frac{1}{Eh}\bar{H}^0 , \qquad \mathbb{C}_b^{-1} := \frac{12}{Eh^3}\bar{H}^0 , \qquad \mathbb{C}_s := Gh\kappa a^0 , \tag{2.37}$$

where

$$\bar{H}^0 := \begin{bmatrix} (a_{11}^0)^2 & -\nu a_{11}^0 a_{12}^0 + (1+\nu)(a_{12}^0)^2 & a_{11}^0 a_{22}^0 \\ & (a_{22}^0)^2 & a_{22}^0 a_{12}^0 \\ \text{SYMM.} & & \tfrac{1}{2}(1-\nu)(a_{12}^0)^2 + \tfrac{1}{2}(1+\nu)a_{11}^0 a_{22}^0 \end{bmatrix} . \tag{2.38}$$

By taking variations of $\Pi : \mathcal{V}_r \times [L_2(\mathcal{A})]^2 \times \mathcal{C} \to \mathbb{R}$ relative to $\tilde{r} \in \mathcal{V}_r$ and $\bar{\delta} \in [L_2(\mathcal{A})]^2$, we obtain the following variational equations:

(i) Membrane and bending:

$$G_m(\tilde{n}, \Phi; \delta\tilde{n}) := \int_{\mathcal{A}} \delta\tilde{n}^t[-\mathbb{C}_m^{-1}\tilde{n} + \varepsilon(\Phi)] \, d\mu^0 = 0$$

$$\forall \, \delta\tilde{n}, \delta\tilde{m} \in [L_2(\mathcal{A})]^3 . \tag{2.39}$$

$$G_b(\tilde{m}, \Phi; \delta\tilde{m}) := \int_{\mathcal{A}} \delta\tilde{m}^t[-\mathbb{C}_b^{-1}\tilde{m} + \rho(\Phi)] \, d\mu^0 = 0$$

(ii) Tranverse shear: Because of the Hu-Washizu type of variational formulation, we have

$$\int_{\mathcal{A}} \delta\bar{\gamma}^{t}[\mathbb{C}_{s}(\bar{\gamma} - \bar{\gamma}^{0}) - \tilde{q}]\,d\mu^{0} = 0\,, \qquad \int_{\mathcal{A}} \delta\tilde{q}^{t}[\delta(\Phi) - \bar{\delta}]\,d\mu^{0} = 0\,. \qquad (2.40a,b)$$

In what follows, we restrict our attention to fields of the form

$$\tilde{q} := \mathbb{C}_{s}(\bar{\gamma} - \bar{\gamma}^{0}) \equiv \mathbb{C}_{s}\bar{\delta}\,. \qquad (2.41)$$

Consequently, (2.40a) is identically satisfied and (2.40b) reduces to the condition

$$G_{s}(\bar{\delta},\,\Phi;\delta\bar{\delta}) = \int_{\mathcal{A}} \delta\bar{\delta}^{t}\mathbb{C}_{s}[\delta(\Phi) - \bar{\delta}]\,d\mu^{0} = 0\,, \qquad (2.42)$$

which furnishes a compatibility condition for the assumed strain field $\bar{\gamma}$ and $\bar{\delta} = \bar{\gamma} - \bar{\gamma}^{0}$ first derived in [23].

Variational equations (2.39) and (2.41)–(2.42), along with the weak form of the equilibrium equations, furnish the variational framework within which we develop our finite element formulation.

3. Mixed approximation and conceptual solution procedure

The mixed variational formulation of the static boundary value problem is posed as follows.

PROBLEM (*M*): Find the configuration $\Phi = (\varphi,\,t) \in \mathcal{C}$, the stress resultants $\tilde{r} = (\tilde{n},\,\tilde{q},\,\tilde{m}) \in \mathcal{V}_{r}$ and the (assumed) transverse shear strain field $\bar{\delta} \in [L_{2}(\mathcal{A})]^{2}$, such that

$$G(\tilde{r},\,\Phi;\delta\Phi) = 0 \quad \forall \delta\Phi = (\delta\varphi,\,\delta t) \in T_{\Phi}\mathcal{C}\,,$$

$$G_{m}(\tilde{n},\,\Phi;\delta\tilde{n}) = 0 \quad \forall \delta\tilde{n} \in [L_{2}(\mathcal{A})]^{3}\,,$$

$$G_{b}(\tilde{m},\,\Phi;\delta\tilde{m}) = 0 \quad \forall \delta\tilde{m} \in [L_{2}(\mathcal{A})]^{3}\,, \qquad (3.1)$$

$$G_{s}(\bar{\delta},\,\Phi;\delta\bar{\delta}) = 0 \quad \forall \delta\bar{\delta} \in [L_{2}(\mathcal{A})]^{2}\,,$$

$$\tilde{q} := \mathbb{C}_{s}(\bar{\gamma} - \bar{\gamma}^{0})\,.$$

The first step in the solution of Problem (M) is the reduction to a generalized displacement model in which the variables $\tilde{r} \in \mathcal{V}_{r}$ and $\bar{\delta} \in [L_{2}(\mathcal{A})]^{2}$ are eliminated at the element level by introducing finite element approximations discontinuous between elements. Accordingly, we obtain the generalized displacement problem:

PROBLEM (*D*): Find the configuràtion $\Phi = (\varphi,\,t) \in C$, such that

$$\bar{G}(\Phi;\delta\Phi) = 0 \quad \forall \delta\Phi = (\delta\varphi,\,\delta t) \in T_{\Phi}\mathcal{C}\,. \qquad (3.2)$$

The reduction process from Problem (M) to Problem (D) is patterned after our interpolation scheme for the membrane, bending and transverse shear fields in the linearized theory, as

discussed in detail in Part II. The appropriate modifications of these procedures to account for nonlinear geometric effects are presented in a detailed step-by-step implementational procedure in Appendix C (Section C.2.2 for membrane, C.2.3 for transverse shear, and C.2.4 for bending).[1]

Conceptually, the solution to Problem (D) is obtained through a Newton–Kantorovitch iteration scheme as follows:

Newton iterative scheme. Given $\Phi^k = (\varphi^k, t^k) \in \mathscr{C}$,

(i) Solve the linearized problem:

$$D[\bar{G}(\Phi^k; \delta\Phi)] \cdot \Delta\Phi^k + \bar{G}(\Phi^k; \delta\Phi) = 0 , \qquad (3.3)$$

to obtain $\Delta\Phi^k \in T_{\Phi^k}\mathscr{C}$.

(ii) Update the configuration $\Phi^k \mapsto \Phi^{k+1} \in \mathscr{C}$ with $\Delta\Phi^k$.

(iii) Check convergence. If $\bar{G}(\Phi^{k+1}; \delta\Phi) \neq 0$, set $k \mapsto k+1$ and go to (i).

Existing convergence results of Newton type of methods for elasticity are typically based on the implicit function theorem. For related results see [24]. The numerical implementation of the solution procedure outlined above involves the following steps.

(i) *Approximation.* Galerkin projection of the problem onto a finite-dimensional manifold $\mathscr{C}^h \subset \mathscr{C}$. The interpolation of the 'mid-surface' part φ and $\Delta\varphi$ is accomplished in the standard fashion by means of the isoparametric concept. However, as discussed in Section 4 below, the interpolation of the 'director part' is non-standard, and must be chosen in such a way as to ensure that t^h and Δt^h remain, or approximately remain, in S^2 and $T_t S^2$, respectively.

(ii) *Update.* Given the configuration $\Phi^k \in \mathscr{C}^h$, and the incremental vector field $\Delta\Phi^k = (\Delta\varphi^k, \Delta t^k) \in T_{\Phi^k}\mathscr{C}^h$, the configuration update procedure must ensure that the updated configuration Φ^{k+1} does in fact remain in $\mathscr{C}^h \subset \mathscr{C}$. (For convenience, the superscript h has been omitted from quantities identified with the iteration parameter k.) The update procedure is discussed in detail in Section 4.

(iii) *Linearization.* Construction of the consistent tangent operator which is the bilinear form $B : T_{\Phi^k}\mathscr{C}^h \times T_{\Phi^k}\mathscr{C}^h \to \mathbb{R}$ defined as

$$B \equiv D\bar{G}[\Phi^k; (\delta\varphi, \delta t)] \cdot (\Delta\varphi^k, \Delta t^k) := \frac{d}{d\varepsilon}\bigg|_{\varepsilon=0} \bar{G}(\Phi^k_\varepsilon; (\delta\varphi, \delta t)) . \qquad (3.4)$$

Here, $\Phi^k_\varepsilon = (\varphi^k_\varepsilon, t^k_\varepsilon) \in \mathscr{C}^h$ is a one-parameter family of configurations 'tangent' to the variation $(\Delta\varphi^k, \Delta t^k) \in T_{\Phi^k}\mathscr{C}^h$, as discussed in Section 2.1. An example of the consistent tangent operator for a particular interpolation is given in Section 5.

---

[1] Actually, C.2.4 outlines the displacement approximation. A mixed approximation similar to that employed for the membrane field follows identical lines as C.2.2 and hence further details are omitted.

4. Interpolation; exact configuration updates

Our main result in this section is the development of an exact update scheme for the nodal director field. This procedure appears to be canonical.

4.1. Mid-surface interpolation; the discrete update problem

The Galerkin approximation to Problem (D) is based on the iso-parametric concept, and constructed in terms of nodal quantities $(d_A, t_A) \in \mathbb{R}^3 \times S^2$, where $A \in \{1, 2, 3, 4\}$ for the bi-linear QUAD. For the mid-surface, $\varphi : \mathscr{A} \to \mathbb{R}^3$, at any iteration k of the solution procedure, we set

$$S^{h(k)} := \{\varphi^{h(k)} : \square \to \mathbb{R}^3 \mid \varphi^{h(k)}\big|_{\Omega_e} = \sum_{A=1}^{Nen} N^A(\xi, \eta) d_A^k\} . \tag{4.1}$$

Here $\square := \{(\xi, \eta) \in [-1, 1] \times [-1, 1]\}$ denotes the bi-unit square, as shown in Fig. 4.1. Similarly, for the tangent plane, following the isoparametric concept (for background information see, e.g., [25–27]), we set

$$T_{\varphi^h} S^{h(k)} := \{\Delta\varphi^{h(k)} : \square \to \mathbb{R}^3 \mid \Delta\varphi^{h(k)}\big|_{\Omega_e} = \sum_{A=1}^{Nen} N^A(\xi, \eta) \Delta d_A^k\} . \tag{4.2}$$

Here, $N^A(\xi, \eta)$ are the standard bilinear isoparametric shape functions defined as

$$N^A(\xi, \eta) := \tfrac{1}{4}[1 + \xi\xi_A][1 + \eta\eta_A] , \quad A = 1, 2, 3, 4 , \tag{4.3}$$

where $(\xi_A, \eta_A) \in \{(-1, -1); (1, -1); (1, 1); (-1, 1)\}$.

Possible interpolation schemes for the director field are discussed in Section 4.3. Since the Galerkin projection is defined in terms of nodal values, within the context of the discretized version of the Newton solution procedure discussed above, the following problem arises:
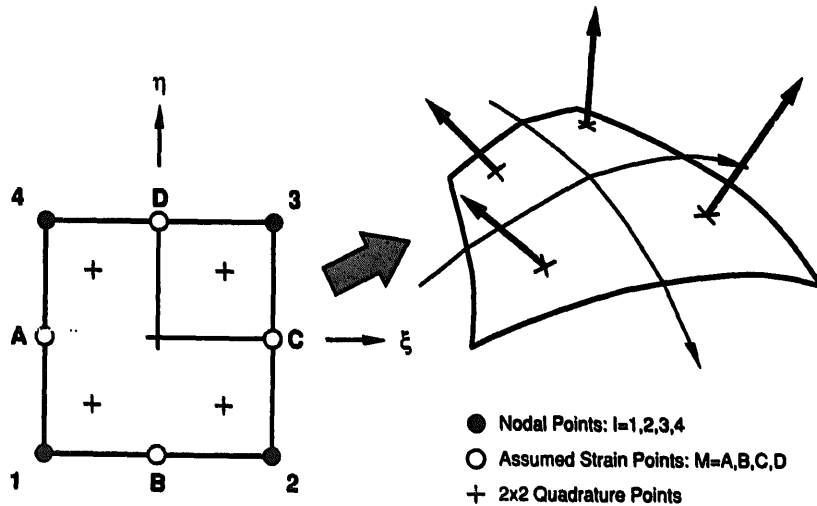

Fig. 4.1. Standard isoparametric bi-unit square, mapped into the shell element configuration.

Discrete update problem.

(i) Given a discrete configuration at the kth-iteration, defined by

$$(d_A^k, t_A^k) \in \mathbb{R}^3 \times S^2 ; \qquad \Lambda_A^k \in SO(3) . \tag{4.4}$$

(ii) Given discrete (nodal) increments

$$(\Delta d_A^k, \Delta T_A^k) \in \mathbb{R}^3 \times T_E S^2 . \tag{4.5}$$

(iii) Obtain (d_A^{k+1}, t_A^{k+1}) in $\mathbb{R}^3 \times S^2$.
(iv) Update $\Lambda_A^k \mapsto \Lambda_A^{k+1} \in SO(3)$.

REMARK 4.1. Observe that the incremental solution is in terms of material director increments $\Delta T_A^k \in T_E S^2$, i.e., in terms of only two degrees of freedom. Here Λ_A^k is the orthogonal matrix that maps E_3 into t_A^k and ΔT_A^k into Δt_A^k. Part of the update problem is to properly update this rotation matrix. Also observe that the exact update procedure for d_A^k is trivially constructed since $\Delta \varphi^k$ and d_A^{k+1} are in $\mathbb{R}^3$; see step (iv) of Box 2.

4.2. Geometrically exact nodal director field update

Geometrically, the update of the nodal director field for given (tangent) director increments is equivalent to tracing the evolution of a point on the unit sphere S^2. Consistent with this

Box 2
Exact update algorithm

(i) Compute spatial director increments

$$\Delta t_A^k = \Lambda_A^k \Delta T_A^k .$$

(ii) Update directors

$$t_A^{k+1} = \exp_{t_A^k} [\Delta t_A^k] := \cos \|\Delta t_A^k\| t_A^k + \frac{\sin \|\Delta t_A^k\|}{\|\Delta t_A^k\|} \Delta t_A^k .$$

(iii) Compute rotation increment matrix

$$\Delta \Lambda_A^k = \cos \|\Delta t_A^k\| 1 + \frac{\sin \|\Delta t_A^k\|}{\|\Delta t_A^k\|} [t_A^k \times \Delta t_A^k]^\wedge$$

$$+ \frac{(1 - \cos \|\Delta t_A^k\|)}{\|\Delta t_A^k\|^2} (t_A^k \times \Delta t_A^k) \otimes (t_A^k \times \Delta t_A^k) .$$

(iv) Update rotation matrix

$$\Lambda_A^{k+1} = \Delta \Lambda_A^k \Lambda_A^k .$$

(v) Update surface configuration

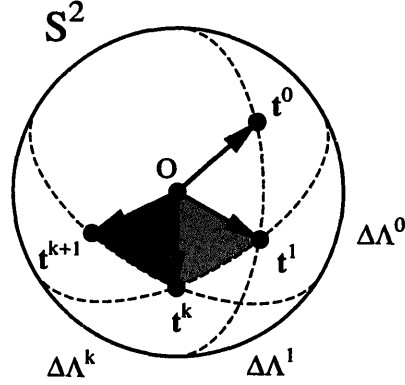$$d_A^{k+1} = d_A^k + \Delta d_A^k .$$

Fig. 4.2. Geometric interpretation of the update procedure for the director field. Each nodal director describes a curve on S^2 composed of arcs of geodesic (i.e., arcs of a great circle).

geometric view, at each iteration k, one updates $t_A^k \in S^2$ for given $\Delta t_A^k \in T_{t_A^k} S^2$ by making use of the exponential map $\exp_{t^k} : T_{t^k} S^2 \to S^2$. The result is a curve composed by arcs of geodesics (maximum circles) on S^2, as illustrated in Fig. 4.2. Such a procedure results in director updates which are exact for arbitrarily large magnitude of the incremental rotation $\Delta t_A^k \in T_{t_A^k} S^2$.

The procedure goes as follows. According to Remarks 2.2 and 4.1 spatial and material director increments are connected through the relation $\Delta t_A^k = \Lambda_A^k \Delta T_A^k$, where $E \mapsto t_A^k = \Lambda_A^k E \in S^2$. Observe that $\Delta t_A^k \in T_{t_A^k} S^2$ since, by construction,

$$t_A^k \cdot \Delta t_A^k = \Lambda_A^k E \cdot \Lambda_A^k \Delta T_A^k = E \cdot \Delta T_A^k = 0 .\tag{4.6}$$

Thus, by Proposition 2.1, use of the exponential map in S^2 given by (2.7), yields the nodal director update formula in Box 2. It can be easily verified that indeed $\|t_A^{k+1}\| = 1$.

Once the nodal director field update is achieved, the orthogonal transformation Λ_A^k is updated as $\Lambda_A^{k+1} = \Delta\Lambda_A^k \Lambda_A^k$, where $\Delta\Lambda_A^k \in SO(3)$ is the unique orthogonal transformation that rotates $t_A^k \in S^2$ to $t_A^{k+1} \in S^2$ without drill, as given by Proposition 2.2. A geometric interpretation of the update procedure, recorded for convenience in Box 2, is given in Fig. 4.3.
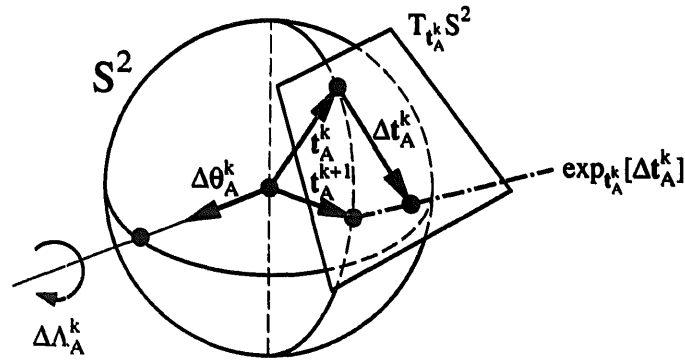

Fig. 4.3. Geometric update procedure in S^2. Nodal directors, which updated by means of the exponential map, rotate by amount $\Delta\Lambda_A^k$.

REMARK 4.2. Observe that the expression in Box 2 for the incremental rotation matrix $\Delta \Lambda_A^k$ is always singularity-free and well-conditioned regardless of the size of the incremental rotation. Identical observations apply to the update formula for the nodal director field. We emphasize that these update formulae are exact.

REMARK 4.3. The exact update formula employed here is identical to employing Rodrigues' formula with the one dependent rotation directly incorporated. Hence, a 2 DOF rotational system is implicitly assumed. The topic of a generalized 3 DOF rotational system is being addressed in a subsequent paper.

4.3. Interpolation of director field (at Gauss points)

The update procedure for the nodal director field summarized in Box 2 is uniquely determined and appears to be canonical. By contrast, given the nodal directors, the interpolations of the director field within the element is not canonically defined and several alternative schemes are possible. We discuss below three of these possible interpolation schemes that result in interpolated director fields which satisfy, to varying degree, the constraints placed by the geometric structure of S^2 on the director and director variations.

Recall that at any iteration k, t_A^k, Λ_A^k and ΔT_A^k are given data. In addition

$$\Delta T_A^k = \Delta \Theta_A^k \times E \quad \Rightarrow \quad \Delta \Theta_A^k = E \times \Delta T_A^k \tag{4.7}$$

and, by definition, $\Delta t_A^k = \Lambda_A^k \Delta T_A^k$ and $\Delta \theta_A^k = \Lambda_A^k \Delta \Theta_A^k$. In the following update procedure examples, different levels of nodal information are used leading to different update procedures for the director field at Gauss points.

Example 4.1. Continuum consistent interpolation

In this example, the incremental director field constrained to lie in $T_{t^k}S^2$, is obtained by isoparametric interpolation with bilinear shape functions as

$$\Delta t^k = \sum_{A=1}^{4} N^A(\xi, \eta) \Delta t_A^k \ . \tag{4.8}$$

The motivation for this interpolation comes from the fact that in the continuum weak form and in the continuum tangent operator, $\delta \varphi$, $\Delta \varphi$, δt and Δt all appear linearly. In the present interpolation, the Gauss point incremental director field vectors are obtained from a linear combination of the nodal incremental director field vectors (in the same manner as the mid-surface position vector is obtained from a linear combination of the nodal position vectors); thus, this interpolation results in a discrete weak form and a discrete tangent operator which is similar to the continuum structure of the equations. Therefore, the discrete equations are obtained simply by substituting interpolation (4.2) and (4.8) into the corresponding continuum equations with no modification.The corresponding weak form is presented in Appendix A, while the discrete tangent operator is presented in Section 5.

Using the nodal update procedure as a guide, the update of the director field is obtained from Δt^k through the use of the exponential map in S^2, i.e.,

$$t^{k+1} = \exp_{t^k} [\Delta t^k] = \cos \|\Delta t^k\| t^k + \frac{\sin \|\Delta t^k\|}{\|\Delta t^k\|} \Delta t^k . \tag{4.9}$$

Differentiation of (4.9) with respect to $\xi^\alpha (\alpha = 1, 2)$ gives the update expression for the director derivatives

$$t^{k+1}_{,\alpha} = \cos \|\Delta t^k\| t^k_{,\alpha} + \left\{ \frac{\sin \|\Delta t^k\|}{\|\Delta t^k\|} (1 - t^k \otimes \Delta t^k) \right.$$

$$\left. + \frac{1}{\|\Delta t^k\|^2} \left(\cos \|\Delta t^k\| - \frac{\sin \|\Delta t^k\|}{\|\Delta t^k\|} \right) \Delta t^k \otimes \Delta t^k \right\} \Delta t^k_{,\alpha} . \tag{4.10}$$

Owing to the simplicity of (4.8)–(4.10), the discrete strain operators and the linearization are relatively simple and easy to implement. However, it is apparent from (4.8) together with (4.9), that $t^k \cdot \Delta t^k \neq 0$. This fact has the consequence that $\|t^{k+1}\| \neq 1$ and $t^{k+1} \cdot t^{k+1}_{,\alpha} \neq 0$ at points other that the nodal points. Although these properties are not satisfied, numerical simulations with this simple update procedure do not indicate a marked loss of accuracy of the converged solution relative to methods, such as Example 4.2, which do satisfy these properties. By noting that in Example 4.2 $\Delta t^k = \Delta \theta^k \times t^k$ and $\|\Delta t^k\| = \|\Delta \theta^k\|$, comparison of (4.12) and (4.13) of Example 4.2 below with (4.8) and (4.9) of Example 4.1 shows that the two procedures are equivalent up to higher order correction terms. The interpolation of Example 4.1 is used in the calculation of the numerical examples of Section 6.

Example 4.2. The full SO(3) update

In this update procedure, the incremental rotation vector, $\Delta \theta^k$, is interpolated with the shape functions from the nodal values as

$$\Delta \theta^k = \sum_{A=1}^{4} N^A(\xi, \eta) \Delta \theta^k_A . \tag{4.11}$$

This procedure is equivalent to interpolating the nodal skew-symmetric incremental rotation matrices. The updated Gauss point director is then obtained by exponentiating the skew-symmetric tensor associated with the axial vector $\Delta \theta^k$ using the exponential map in SO(3) as given in (2.9). Thus, the updated director field is obtained as

$$t^{k+1} = \exp [\Delta \hat{\theta}^k] t^k ,$$

$$\exp [\Delta \hat{\theta}^k] := \cos \|\Delta \theta^k\| 1 + \frac{\sin \|\Delta \theta^k\|}{\|\Delta \theta^k\|} [\Delta \hat{\theta}^k] + \frac{1 - \cos \|\Delta \theta^k\|}{\|\Delta \theta^k\|^2} (\Delta \theta^k \otimes \Delta \theta^k) . \tag{4.12}$$

It can be verified that $\|t^{k+1}\| = 1$. The director field derivative update formula follows from differentiating (4.12) and is given as

$$t^{k+1}_{,\alpha} = \exp [\Delta \hat{\theta}^k] t^k_{,\alpha} + h^k_\alpha \times t^{k+1} , \tag{4.13a}$$

where h_α^k is the axial vector of the derivative of the exponential map; i.e.,

$$\hat{h}_\alpha^k := \left[\frac{\partial}{\partial \xi^\alpha} \exp \left[\Delta \hat{\theta}^k \right] \right] \exp \left[-\Delta \hat{\theta}^k \right] . \tag{4.13b}$$

It can be shown, see [16], that the following expression for the axial vector, h_α^k, of the derivative of the exponential map in SO(3) holds

$$h_\alpha^k = H(\Delta \theta^k) \Delta \theta_{,\alpha}^h , \tag{4.14a}$$

where $H(\Delta \theta^k)$ is defined as

$$H(\Delta \theta^k) := n \otimes n + \frac{\sin \Delta \theta^k}{\Delta \theta^k} [1 - n \otimes n] + \frac{1}{2} \frac{\sin^2 \left(\frac{1}{2} \Delta \theta^k \right)}{\left(\frac{1}{2} \Delta \theta^k \right)^2} [\Delta \hat{\theta}^k] ,$$

$$n := \frac{\Delta \theta^k}{\|\Delta \theta^k\|} , \qquad \Delta \theta^k := \|\Delta \theta^k\| . \tag{4.14b}$$

This update procedure maintains the properties that $\|t^{k+1}\| = 1$, i.e., $t^{k+1} \in S^2$, $t^k \cdot \Delta t^k = 0$, i.e., $\Delta t^k \in T_{t^k} S^2$ and that $t^{k+1} \cdot t_{,\alpha}^{k+1} = 0$. Because of the nonlinear character of the interpolation (4.11) for the incremental field and the complex nature of (4.12)–(4.14), the discrete strain operators and the subsequent linearization are far more involved than the simple interpolation scheme in Example 4.1. For the present formulation, our numerical simulations do not exhibit a significant increase in performance.

Example 4.3. Material incremental director field interpolation

In Example 4.1, the spatial incremental rotation vectors were interpolated. In this example, the material incremental director field vectors are interpolated. The procedure is as follows:

$$\Delta T^k = \sum_{A=1}^{4} N^A(\xi, \eta) \Delta T_A^k . \tag{4.15a}$$

The spatial incremental director field vector is obtained as

$$\Delta t^k = \Lambda^k \Delta T^k . \tag{4.15b}$$

Note that the Gauss point orthogonal transformation Λ^k, where $t^k = \Lambda^k E$, is required in (4.15) to rotate the material incremental vector to the spatial incremental vector. This rotation tensor is updated in a manner identical to the procedure outlined in Box 2. Since $\Delta T_A^k \cdot E = 0$, it follows that $\Delta t^k \cdot t^k = \sum_{A=1}^{4} N^A \Delta T_A^k \cdot E = 0$. Hence, $\Delta t^k \in T_{t^k} S^2$ and the director field update is performed with the exponential map in S^2 as

$$t^{k+1} = \exp_{t^k} [\Delta t^k] = \cos \|\Delta t^k\| t^k + \frac{\sin \|\Delta t^k\|}{\|\Delta t^k\|} \Delta t^k . \tag{4.16}$$

Equation (4.16) then determines the director field derivative update. By differentiating (4.16) with respect to ξ^α, we obtain

$$t^{k+1}_{,\alpha} = \cos \|\Delta t^k\| t^k_{,\alpha}$$

$$+ \left\{ \frac{\sin \|\Delta t^k\|}{\|\Delta t^k\|} (1 - t^k \otimes \Delta t^k) + \frac{1}{\|\Delta t^k\|^2} \left(\cos \|\Delta t^k\| - \frac{\sin \|\Delta t^k\|}{\|\Delta t^k\|} \right) \Delta t^k \otimes \Delta t^k \right\}$$

$$\times \Lambda^k \Delta T^k_{,\alpha} - \frac{\sin \|\Delta t^k\|}{\|\Delta t^k\|} (t^k_{,\alpha} \cdot \Delta t^k) t^k \ . \tag{4.17}$$

This procedure appears conceptually consistent. In numerical simulations with initially flat geometries, this update scheme produces exceptionally good results. For example, in the 360 degree roll-up of a cantilevered beam, the exact rotation field is obtained for any number of elements, including the case of a single bi-linear element. Unfortunately, numerical simulations involving initial curvature do not show the same outstanding results.

REMARK 4.4. The discrete strain operators are obtained, for a given choice of $\delta\varphi$ and δt (or δT), by substituting these interpolations into the expression for the static weak form $G(\tilde{r}, \Phi; \delta\Phi) = 0$ in (3.2). We observe that these interpolations are nonlinear. Consequently, the linearization and interpolation processes do not commute. It follows that the tangent operator consistent with the discrete problem is obtained by linearization of the discrete tangent operator. The result again depends on the particular interpolation used. This is considered in detail next. It is essential to observe that this result does not coincide with the result obtained by substitution of the interpolations in the expression for the tangent operator of the exact continuum problem given in Part I.

5. Linearization; tangent operator

In this section, we construct the discrete consistent tangent operator $D\bar{G}(\Phi^k; \delta\Phi) \cdot \Delta\Phi^k$ in the Newton solution procedure (3.3) by taking the directional derivative of the discrete weak form $\bar{G}(\Phi^k; \delta\Phi)$ at configuration $\Phi^k = (\varphi^k, t^k) \in \mathcal{C}^h$ in the direction of the variation $\Delta\Phi^k = (\Delta\varphi^k, \Delta t^k) \in T_{\Phi^k}\mathcal{C}^h$. This yields a bilinear form mapping $T_{\Phi^k}\mathcal{C}^h \times T_{\Phi^k}\mathcal{C}^h$ into $\mathbb{R}$. It is conventional practice to split the tangent operator into material and geometric parts, denoted by $D\bar{G}_M \cdot \Delta\Phi^k$ and $D\bar{G}_G \cdot \Delta\Phi^k$ respectively, as

$$D\bar{G}(\Phi^k; \delta\Phi) \cdot \Delta\Phi^k = D\bar{G}_G(\Phi^k; \delta\Phi) \cdot \Delta\Phi^k + D\bar{G}_M(\Phi^k; \delta\Phi) \cdot \Delta\Phi^k \ . \tag{5.1}$$

The geometric part results from variations in the geometry while holding the material constant, whereas the material part results from variations in the material while holding the geometry constant, as discussed further on.

In what follows, we consider exclusively the mid-surface interpolation (4.1) and the incremental director field interpolation discussed in Example 4.1. As noted in Remark 4.3, linearization and discretization generally do not commute. This lack of commutativity is the

direct result of the choice of interpolation. In the present case, however, since the incremental director field enters linearly in the tangent operator and is interpolated linearly, the two processes do commute.

To further simplify our notation, we rewrite the weak form in Box 1 as

$$G(\tilde{r}, \Phi; \delta\Phi) := \int_{\mathscr{A}} \mathbb{B} \begin{bmatrix} \delta\varphi \\ \delta T \end{bmatrix} \cdot \tilde{r} \, d\mu^0 - G_{ext}(\delta\Phi) , \tag{5.2}$$

where we have set

$$\mathbb{B} = \begin{bmatrix} \mathbb{B}_m & \mathbf{0}_{3\times 2} \\ \mathbb{B}_{sm} & \mathbb{B}_{sb} \\ \mathbb{B}_{bm} & \mathbb{B}_{bb} \end{bmatrix}_{8\times 5} . \tag{5.3}$$

5.1. The material tangent operator

The material part of the tangent operator is obtained from (5.2) by holding $\mathbb{B}$ fixed while taking the directional derivative at configuration $\tilde{\Phi} \in \mathscr{C}$ in the direction $\Delta\Phi \in T_\Phi \mathscr{C}$, i.e., by holding the geometry constant. Accordingly, we set

$$D_M \bar{G}(\Phi; \delta\Phi) \cdot \Delta\Phi = \int_{\mathscr{A}} \mathbb{B} \begin{bmatrix} \delta\varphi \\ \delta T \end{bmatrix} \cdot (D\tilde{r} \cdot \Delta\Phi) \, d\mu^0 . \tag{5.4}$$

Making use of the directional derivative formula one obtains

$$D\tilde{r} \cdot \Delta\Phi = \mathbb{C}\mathbb{B} \begin{bmatrix} \Delta\varphi \\ \Delta T \end{bmatrix} , \tag{5.5}$$

where $\mathbb{C}$ is the elasticity tensor. Substitution of (5.5) into (5.4) yields

$$D_M \bar{G}(\Phi; \delta\Phi) \cdot \Delta\Phi = \int_{\mathscr{A}} \begin{bmatrix} \delta\varphi \\ \delta T \end{bmatrix}^t \mathbb{B}^t \mathbb{C}\mathbb{B} \begin{bmatrix} \Delta\varphi \\ \Delta T \end{bmatrix} d\mu^0 . \tag{5.6}$$

By substituting interpolations (4.2) and (4.8) into (5.6), along with the interpolation resulting from the assumed transverse shear field, with the notation of Appendix A, the discrete material part of the tangent operator is written as

$$D_M \bar{G}(\Phi; \delta\Phi) \cdot \Delta\Phi$$

$$= \sum_{A=1}^{4} \sum_{B=1}^{4} \int_{\mathscr{A}} \{[B_m^A \delta\varphi_A]^t + [B_{sm}(\delta\varphi) + B_{sb}(\delta T)]^t + [B_{bm}^A \delta\varphi_A + B_{bb}^A \delta T_A]^t\}$$

$$\times \mathbb{C}\{[B_m^B \Delta\varphi_B] + [B_{sm}(\Delta\varphi) + B_{sb}(\Delta T)] + [B_{bm}^B \Delta\varphi_B + B_{bb}^B \Delta T_B]\} \, d\mu^0 . \tag{5.7}$$

Observe, that the iteration parameter k has been omitted to simplify the notation.

5.2. The geometric tangent operator

The geometric part of the tangent operator results from holding the material resultants $\tilde{r}$ constant while linearizing $\mathbb{B}$; accordingly, from (5.2), we obtain, in components

$$D\bar{G}_G(\boldsymbol{\Phi}; \delta\boldsymbol{\Phi}) \cdot \Delta\boldsymbol{\Phi} = \int_{\mathscr{A}} [\tilde{n}^{\alpha\beta}\Delta(\delta\varepsilon_{\alpha\beta}) + \tilde{q}^{\alpha}\Delta(\delta\gamma_{\alpha}) + \tilde{m}^{\alpha\beta}\Delta(\delta\kappa_{\alpha\beta})]\bar{J}\,\mathrm{d}\mu^0 , \qquad (5.8)$$

where, by making use of notation (2.29), we have set

$$\begin{bmatrix} \Delta(\delta\varepsilon(\boldsymbol{\Phi})) \\ \Delta(\delta\delta(\boldsymbol{\Phi})) \\ \Delta(\delta\rho(\boldsymbol{\Phi})) \end{bmatrix} := \frac{\mathrm{d}}{\mathrm{d}\varepsilon} \begin{Bmatrix} \delta\varepsilon(\boldsymbol{\Phi}_\varepsilon) \\ \delta\delta(\boldsymbol{\Phi}_\varepsilon) \\ \delta\rho(\boldsymbol{\Phi}_\varepsilon) \end{Bmatrix}_{\varepsilon=0} , \qquad (5.9)$$

with $\boldsymbol{\Phi}_\varepsilon|_{\varepsilon=0} = \boldsymbol{\Phi}$ and $[\mathrm{d}/\mathrm{d}\varepsilon]_{\varepsilon=0}\,\boldsymbol{\Phi}_\varepsilon = \Delta\boldsymbol{\Phi}$. Note again that the iteration superscript k has been omitted from all quantities in the tangent operator although it is implicitly implied. We refer to Appendix B for the details involved in the computation of (5.9), and simply note here that the individual terms in the integrand of (5.5) can be expressed as follows (sums over $\alpha, \beta = 1, 2$ are implied):

$$\tilde{n}^{\alpha\beta}\Delta(\delta\varepsilon_{\alpha\beta}) = \sum_{A=1}^{4} \sum_{B=1}^{4} \delta\varphi_A^t [\tilde{n}^{\alpha\beta} N_{,\alpha}^A N_{,\beta}^B \mathbf{1}]\Delta\varphi_B ,$$

$$\tilde{m}^{\alpha\beta}\Delta(\delta\kappa_{\alpha\beta}) = \sum_{A=1}^{4} \sum_{B=1}^{4} \{\delta\varphi_A^t [\tilde{m}^{\alpha\beta} N_{,\alpha}^A N_{,\beta}^B \bar{\Lambda}_B]\Delta T_B + \delta T_A^t [\tilde{m}^{\alpha\beta} N_{,\beta}^A N_{,\alpha}^B \bar{\Lambda}_A^t]\Delta\varphi_B\}$$

$$- \sum_{A=1}^{4} \delta T_A^t [\tilde{m}^{\alpha\beta}(\varphi_{,\alpha} \cdot t_A) N_{,\beta}^A \mathbf{1}]\Delta T_A . \qquad (5.10)$$

At this point we recall from Remark 2.2 that the five-degree-of-freedom formulation is obtained by introducing the orthogonal transformations $\bar{\Lambda}_A$ and setting $\delta t_A = \bar{\Lambda}_A \delta T_A$ and $\Delta t_A = \bar{\Lambda}_A \Delta T_A$. Without loss of generality we assume that $E \equiv E_3$. Then, the requirement $\delta T_A \cdot E = \Delta T_A \cdot E = 0$ is enforced by restricting δT_A and ΔT_A to have components relative to E_1 and E_2 only. Due to the assumed strain interpolation for the shear strains, the term $\tilde{q}^{\alpha}\Delta(\delta\gamma_{\alpha})$ follows from (B.7) in Appendix B. Let

$A = \tfrac{1}{4}$

$$\times \begin{bmatrix} [-\tilde{q}^1(1-\eta) - \tilde{q}^2(1-\xi)]\bar{\Lambda}_1 & -\tilde{q}^1(1-\eta)\bar{\Lambda}_2 & 0 & -\tilde{q}^2(1-\xi)\bar{\Lambda}_4 \\ \tilde{q}^1(1-\eta)\bar{\Lambda}_1 & [\tilde{q}^1(1-\eta) - \tilde{q}^2(1+\xi)]\bar{\Lambda}_2 & -\tilde{q}^2(1+\xi)\bar{\Lambda}_3 & 0 \\ 0 & \tilde{q}^2(1+\xi)\bar{\Lambda}_2 & [\tilde{q}^1(1+\eta) + \tilde{q}^2(1+\xi)]\bar{\Lambda}_3 & \tilde{q}^1(1+\eta)\bar{\Lambda}_4 \\ \tilde{q}^2(1-\xi)\bar{\Lambda}_1 & 0 & -\tilde{q}^1(1+\eta)\bar{\Lambda}_3 & [-\tilde{q}^1(1+\eta) + \tilde{q}^2(1-\xi)]\bar{\Lambda}_4 \end{bmatrix} ,$$

$$(5.11)$$

$$D = \frac{1}{4} \begin{bmatrix} [\tilde{q}^1(1-\eta)(^2\varphi_{,1} \cdot t_1) \\ + \tilde{q}^2(1-\xi)(^1\varphi_{,2} \cdot t_1)]\mathbf{1} \\ \\ [\tilde{q}^1(1-\eta)(^2\varphi_{,1} \cdot t_2) \\ + \tilde{q}^2(1+\xi)(^3\varphi_{,2} \cdot t_2)]\mathbf{1} \\ \\ [\tilde{q}^1(1+\eta)(^4\varphi_{,1} \cdot t_3) \\ + \tilde{q}^2(1+\xi)(^3\varphi_{,2} \cdot t_3)]\mathbf{1} \\ \\ [\tilde{q}_1(1+\eta)(^4\varphi_{,1} \cdot t_4) \\ + \tilde{q}^2(1-\xi)(^1\varphi_{,2} \cdot t_4)]\mathbf{1} \end{bmatrix} . \qquad (5.12)$$

The shear contribution to the geometric tangent operator becomes

$$\tilde{q}^{\alpha}\Delta(\delta\gamma_{\alpha}) = \begin{bmatrix} \delta\varphi_1 \\ \delta\varphi_2 \\ \delta\varphi_3 \\ \delta\varphi_4 \end{bmatrix}^{t} A \begin{bmatrix} \Delta T_1 \\ \Delta T_2 \\ \Delta T_3 \\ \Delta T_4 \end{bmatrix} + \begin{bmatrix} \delta T_1 \\ \delta T_2 \\ \delta T_3 \\ \delta T_4 \end{bmatrix}^{t} A^{t} \begin{bmatrix} \Delta\varphi_1 \\ \Delta\varphi_2 \\ \Delta\varphi_3 \\ \Delta\varphi_4 \end{bmatrix} - \begin{bmatrix} \delta T_1 \\ \delta T_2 \\ \delta T_3 \\ \delta T_4 \end{bmatrix}^{t} D \begin{bmatrix} \Delta T_1 \\ \Delta T_2 \\ \Delta T_3 \\ \Delta T_4 \end{bmatrix}.$$ (5.13)

REMARK 5.1. The linearization considered here is for the full displacement formulation. The linearization procedure for the mixed formulation follows an identical procedure and is not considered in detail. An example of the linearization for the mixed membrane formulation is given in Appendix C.

REMARK 5.2. In addition to producing asymptotically quadratic rates of convergence in a Newton iteration, the exact closed form expressions for the tangent operator (presented above) play a central role in the bifurcation analysis of structures. The use of an incorrect or approximate tangent stiffness may lead to erroneous results in detection of bifurcation and limit points.

6. Numerical simulations

The applicability of the proposed theory and the performance of the accompanying finite element implementation are assessed by means of numerical simulations that encompass a wide spectrum of problems involving large rotations, finite strains, buckling and post-buckling analyses. True Newton iterations (i.e., using the exact tangent at every iteration) are used in all simulations. The results are compared with several formulations from the literature, as well as with experimental and classical solutions where available. Table 6.1 lists some of the well-known formulations used in our numerical comparisons, and the abbreviations that will be used to denote them henceforth.

Table 6.1
Listing of some standard shell elements

Name	Description
4-ANS	Bi-linear assumed natural strain element, with full integration, Stanley [7] and Park and Stanley [28].
4-RSDS	Bi-linear resultant stress degenerated shell element, with uniform reduced integration and stabilization, Liu et al. [8].
4-SRI	Bi-linear degenerated shell element, with selective reduced integration, Hughes and Liu [5, 6].
4-URI	Bi-linear degenerated shell element, with uniformly reduced integration.
8-SER	Bi-quadratic serendipity element, with uniformly reduced integration, Ahmad et al. [2].
9-HET	Bi-quadratic heterosis element, with selective reduced integration, Hughes and Cohen [29].
9-ANS	Bi-quadratic assumed natural strain element, with full integration, Stanley [7] and Park and Stanley [28].

6.1. Illustrative large deformation problems

We begin by considering four large deformation problems that demonstrate the ability of the formulation to model accurately the effects of large rotations.

6.1.1. Roll-up of a clamped beam

An initially flat shell clamped on one end is subjected to a bending moment on the other end. This classical elastica problem has gained considerable popularity as a benchmark problem for large deformation analysis. The analytical solution corresponds to a beam 'rolled-up' into a circular arc of radius ρ given by the classical formula

$$1/\rho = M/EI , \tag{6.1}$$

where M is the applied end moment. For $M = 2\pi EI/L$, where L is the length of the beam, the beam rolls up into a complete circle. In this simulation, the material properties are chosen as $E = 12 \times 10^6$ and $\nu = 0$. We assume length $L = 10$, width $w = 1$ and thickness $t = 0.1$. To test the singularity-free nature of our parametrization, we investigate the case in which the beam is rolled-up in a single load step (i.e., $\theta = 2\pi$) using a mesh consisting of 25 elements. Figure 6.1.1 depicts the original and deformed configurations. The agreement between the computed results and the exact solution given by (6.1) is excellent.

6.1.2. In-plane bending of a beam; mesh distortion

This problem serves to demonstrate the performance of the membrane interpolation and its insensitivity to mesh distortion. A cantilever beam subjected to an end load is modeled using a 10 element mesh. Subsequently, the mesh is arbitrarily distorted to obain irregular elements with high aspect ratios (see Fig. 6.1.2). The material properties used for this problem are $E = 10 \times 10^6$ and $\nu = 0.3$, the beam length is $L = 1.0$ and the width and thickness are $w = t = 0.1$. The initial and deformed configurations for both meshes are shown in Fig. 6.1.2(a). A plot of the load–deflection curve for the tip displacement for the two meshes is shown in Fig. 6.1.2(b). Inspection of these figures reveals that the results are essentially identical for both meshes and exhibit almost no sensitivity to mesh distortion.
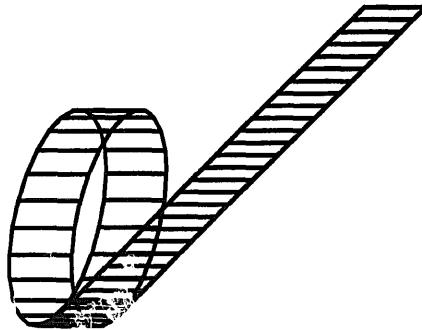

Fig. 6.1.1. Results for the 'roll-up' of a clamped beam. Original and deformed meshes for the end rotation $\theta = 2\pi$ in the exact solution of applied moment loading.
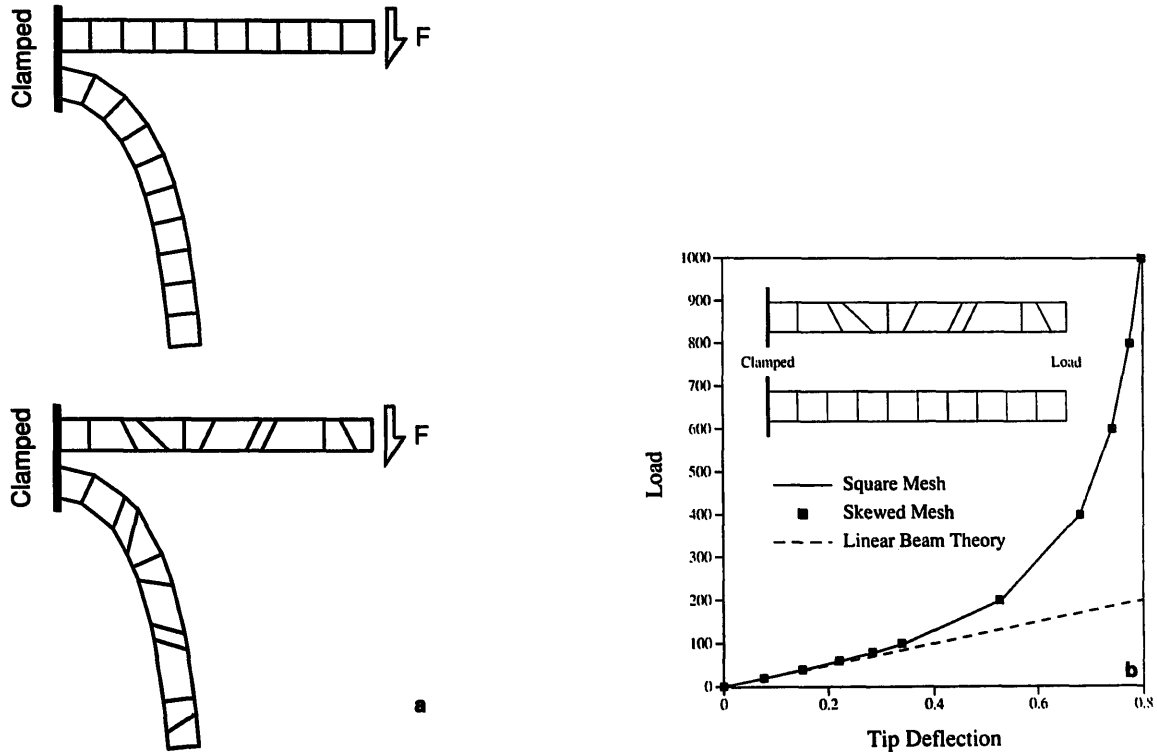
Fig. 6.1.2. (a) Initial and deformed mesh configurations using a square and arbitrarily distorted mesh to discretize the in-plane beam bending problem. Deformations are plotted without any magnification. (b) Load deflection curve for the in-plane bending of a cantilevered beam. Both the square and skew meshes were used to obtain this plot in ten loads steps.

6.1.3. Torsion of a flat plate strip

The purpose of this example is to demonstrate the ability of the formulation to capture large rotations and displacements and, at the same time, illustrate the robustness of the numerical implementation. A torsional moment is applied to the end of an initially flat plate strip, leading to a relative torsional rotation of $\approx 180°$. The initial and deformed mesh configurations are shown in Fig. 6.1.3. The material properties are $E = 12 \times 10^6$ and $\nu = 0.3$, the length is $l = 1.0$, the width is $w = 0.25$ and the thickness is $t = 0.1$. Remarkably, the final configuration shown in Fig. 6.1.3 is attained in three load-steps.

6.1.4. Pinched hemispherial shell; finite strain version

The pinched hemisphere problem, a popular benchmark problem for linear shell analysis, is concerned with the (nearly inextensional) deformation of a hemispherical shell, with an 18° hole at the top, under the action of two inward and two outward forces 90° apart. Symmetry conditions are used on this problem and only one quadrant needs to be modeled. The material properties are $E = 6.825 \times 10^7$ and $\nu = 0.3$, the radius is $R = 10$ and the thickness is $t = 0.04$. Again, to illustrate the large deformation capabilities of the formulation, the loads are increased by two orders of magnitude in order to obtain deflections of $\approx 60\%$ of the initial radius. It should be noted that in contrast with the linear case, the deflections under the loads are not equal. A plot of the pinching load values versus the deflection under the corresponding
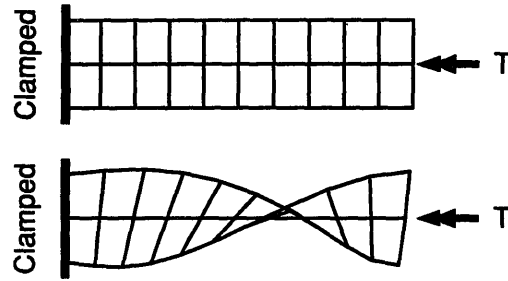
Fig. 6.1.3. Initial and deformed mesh configurations for the torsion of a clamped plate strip. Final configuration is arrived at in three loads steps. Deformations are plotted without magnification.
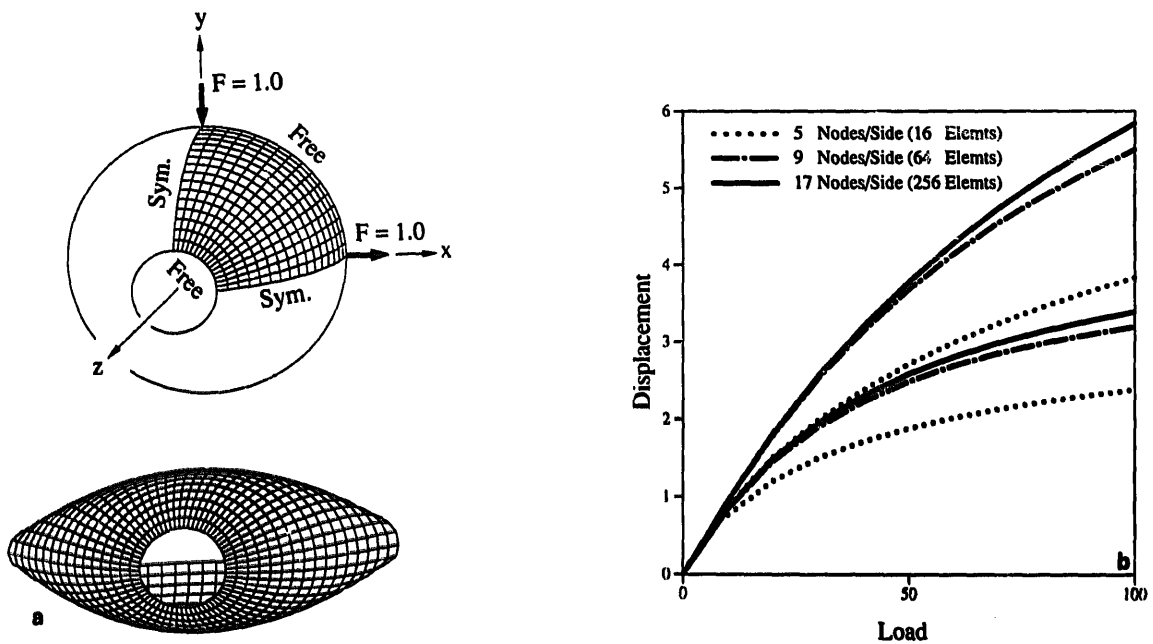

Fig. 6.1.4. (a) Initial and deformed mesh configurations for the large strain version of the pinched hemisphere problem. The final configuration, involving deformations of ≈ 60% of the radius, is arrived at using ten load steps. Deformations are plotted without magnification. (b) Deflection–load plots for the different mesh configurations used to model the large strain version of the pinched hemisphere problem. In contrast with the linear problem, the displacements under the pinching loads are not equal. The three top curves correspond to the displacements under the vertical loads, while the lower curves represent the displacements under the horizontal loads.

pinching load is shown in Fig. 6.1.4(b) for different mesh configurations. Figure 6.1.4(a) shows the initial and deformed mesh configurations without any magnification of the deformations. This calculation was carried out in ten load steps.

REMARK 6.1. It is well known that for problems involving finite strains, the effects of thickness change play an important role in the solution. The extension of the present formulation to account for these effects is considered in detail in Part IV.

6.2. Buckling eigen-pair analysis

We further assess the performance of the proposed formulation by considering four problems concerned with buckling analysis. Results are presented both for the critical buckling loads (eigenvalues) and for the associated mode shapes (eigenvectors). In the stability analysis, two different approaches can be followed: the classical linearized buckling analysis, and a non-linear buckling analysis that traces the possibly nonlinear response of the structure up to the bifurcation (or limit load) point.

(i) The linearized buckling analysis is based on the assumption that the problem will behave linearly until the point of bifurcation and the geometric stiffness will, therefore, be a linear function of the load level. This assumption leads to the following linearized eigen-problem,

$$[K_m|_{\Phi=\text{iden}} = \lambda K_g|_{\Phi=\text{iden}}]\psi = 0, \tag{6.3a}$$

where K_m and K_g are the material and geometric tangent stiffness matrices evaluated at the reference configuration, and λ and ψ are the buckling load and associated linear buckling mode.

(ii) On the other hand, in the non-linear buckling analysis, the load/deflection path (principal load path) is traced until a limit or bifurcation point is detected; i.e., until a configuration $\bar{\Phi} \in \mathscr{C}$ is reached in which the tangent stiffness matrix becomes singular and satisfies the eigenvalue problem

$$[K_T|_{\Phi=\bar{\Phi}} + w\mathbf{1}]\psi = 0 \quad \text{for } w = 0. \tag{6.3b}$$

Thus, it is precisely at configuration $\bar{\Phi}$ for which the tangent stiffness matrix is singular, and not at $\Phi = \text{iden}$, where the eigenvalue analysis is performed. The singularity of the stiffness matrix is detected by monitoring the pivots in the factorization of the stiffness matrix and checking for sign changes. Alternatively, the bifurcation point can be arrived at by employing an extended system of equations (see, i.e., [30]).

6.2.1. Simply-supported plate

A simply-supported plate is subjected to an in-plane compressive load N as shown in Fig. 6.2.1. The material properties used in this example are $E = 10 \times 10^6$ and $\nu = 0.3$, the side length is $a = 10$ and the thickness is $t = 0.1$. Symmetry boundary conditions are employed to model one quadrant of the plate and a linearized buckling analysis is performed. The closed-form expression for the linearized buckling load for this problem is given by $N_{cr} = 4\pi^2 D/l^2$, and the associated buckling mode corresponds to a half-sine wave in both the x and y directions. Figure 6.2.1 shows the convergence of the lowest buckling load, normalized relative to the exact solution, along with a comparison with several other well-known formulations. The proposed approach exhibits the best performance among the formulations shown.

6.2.2. In-plane bending of an L-shaped plate strip

We consider the stability analysis of an L-shaped flat plate which is clamped on one end and subjected to an in-plane load on the other, as shown in Fig. 6.2.2. This problem has been investigated by Argyris et al. [31] and Simo and Vu-Quoc [17, 18] to assess the performance of
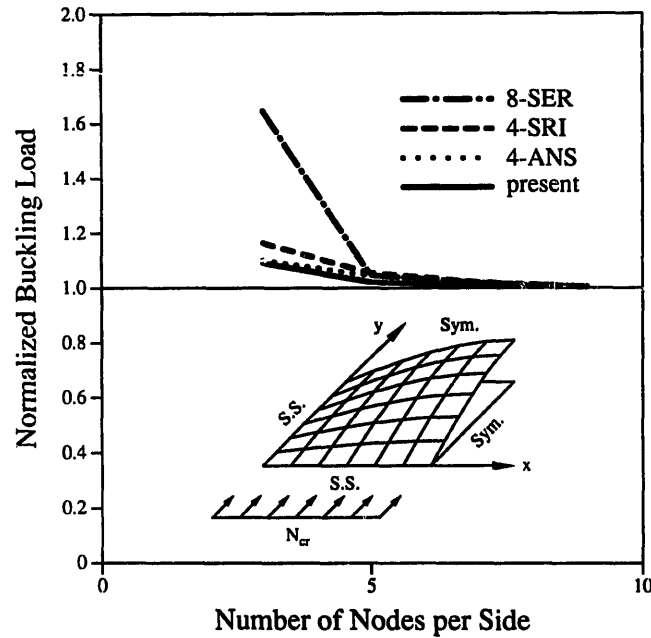
Fig. 6.2.1. Problem definition and convergence results for the buckling of a simply-supported plate problem. Linearized buckling analysis is performed to obtain the critical buckling load for several mesh configurations and loads are normalized with the exact linear buckling load.

Fig. 6.2.2. Convergence plots for the non-linear buckling load versus the number of elements for the analysis of a built-in right angle frame problem. The top curve corresponds to the critical load usually found in the literature. The bottom curve corresponds to the buckling load when the load direction is reversed, which is of lower magnitude.

nonlinear rod elements. The material properties for this problem are Young's modulus $E = 71240$ and Poisson's ratio $\nu = 0.31$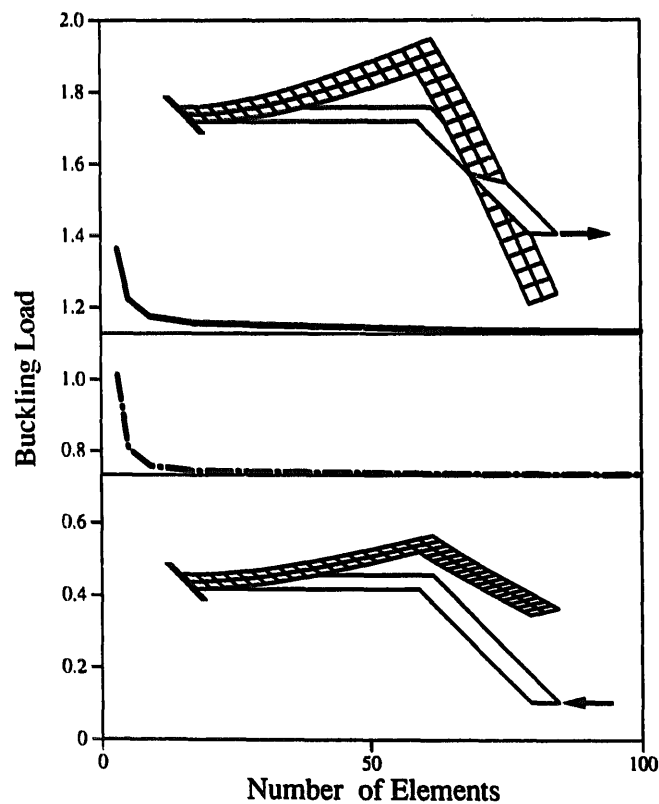, the edge length is $l = 240$, the edge width is $w = 30$ and the thickness is $t = 0.6$. Interestingly, this problem exhibits two different bifurcation points, depending on the load direction. The first bifurcation point, shown in the upper part of Fig. 6.2.2, is the one reported in the literature. The second bifurcation point, associated with a lower load value of opposite sign, is shown in the lower part of Fig. 6.2.2.

The results for the first bifurcation load, obtained using an extended system of equations as in [30], are shown in Table 6.2.2, and the convergence of the value of the critical loads obtained with this formulation for the two different load directions are shown in Fig. 6.2.2. Excellent agreement is found between the present approach and the geometrically exact rod model in [16].

6.2.3. Effect of L/R ratio on the buckling load of an axially compressed cylinder; clamped, simply-supported and free end boundary conditions

The buckling of axially compressed cylinders is a classical problem extensively studied from an analytical, experimental and numerical perspective in the literature; see, e.g., the recent review account of Bushnell [33]. It is a classical result that, except for the case of free boundaries, the magnitude of the buckling load is highly insensitive to the edge boundary conditions provided that 'the length of the cylinder is not small (say $L > 2R$)' [34, p. 464]. On the other hand, for extremely small values of the length to radius ratio, L/R, the behavior of the shell closely resembles that of a collection of small meridional strips, and the buckling load tends to the classical Euler's formula for a strut [34, p. 466]. In this latter case, the effect of boundary conditions becomes crucial. For instance, the critial load for the very short simply-supported cylinder, which is associated with a reticulated mode shape with one half-sine wave in the axial direction and several waves in the circumferential direction, will be much smaller than the buckling load corresponding to the clamped case. The buckling mode shapes for the clamped short cylinder case are axisymmetric.

For long cylinders, an approximate solution for the critical load which is independent of length, referred to herein as the classical solution, is given by (see e.g.,[34, p. 465])

$$P_{cl} \approx Et^2/R\sqrt{3(1 - \nu^2)}.$$

(6.4)

This approximation is valid only for long cylinders with fixed end boundary conditions (clamped or simply-supported). The eigen-modes associated with these critical loads can be axisymmetric, reticulated or 'diamond' shaped. Hoff and Soong [35], however, show analytically that the buckling loads for the boundary condition of free ends is $0.38 \times P_{cl}$, correspond-

Table 6.2.2
In-plane buckling loads for a right-angle frame

Reference	Type	Elmts	Load
Simo et al. [32]	Beam	20	1.090
Argyris et al. [31]	Beam	20	1.088
Argyris et al. [31]	Shell	63	1.155
present	Shell	68	1.137
Converged solution			1.128

ing to modes of two circumferential sine-waves and no longitudinal waves, which are precluded by the fixed end conditions.

In this simulation, we consider a thin cylinder $(R/t \approx 400)$ and examine the effect of different values of the ratio length L to radius R on the critical load for the different end boundary conditions. A 20×20 mesh is used to model one-eighth of the cylinder, using the appropriate symmetry conditions. The material properties of the shell are $E = 567$ and $v = 0.3$, the cylinder radius is $R = 100$ and the thickness is $t = 0.247$. The results obtained in the simulation for several values of the ratio L/R are presented in Fig. 6.2.3 normalized relative to the classical value of P_{cl} given by (6.4). From this figure, it is readily apparent that the present formulation predicts higher critical loads for short clamped cylinders than short simply-supported cylinders and cylinders with free ends. For long cylinders, the present formulation predicts that critical loads for the clamped and simply-supported cases will converge to the classical approximation, and the free end case will converge to the value reported by Hoff and Soong [35]. Hence, the computed results are in complete agreement with the classical behavior of cylindrical shells, as described before.

6.2.4. *Linearized vs. non-linear buckling analysis; axially compressed cylinder example*

This example is studied by Liu et al. [8] using linearized buckling analysis in their assessment of the performance of the 4-SRI and 4-RSDS degenerated solid elements. A

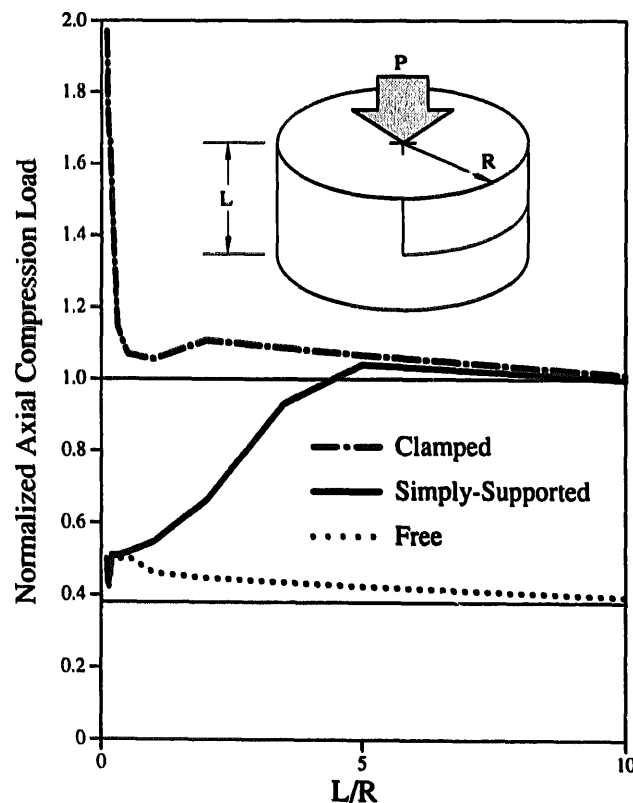Fig. 6.2.3. Effect of length-to-radius ratio L/R on the critical buckling load of an axially compressed cylinder under different boundary conditions. Results are obtained using linearized buckling analysis and normalized with respect to the classical approximation $P_{cl} = Et^2/R\sqrt{3(1 - v^2)}$. A 20×20 mesh is employed to discretize the shaded area using the approximate symmetry boundary conditions.

30 × 14 mesh is used on one-eighth of a cylinder to predict the critical buckling load of the cylinder shown in Fig. 6.2.4(a). The material properties are $E = 567$ and $\nu = 0.3$, radius $R = 100$, length $L = 35.95$ and thickness $t = 0.247$. Four different boundary conditions are investigated:

(a) Free ends, with a shortening displacement applied;
(b) Free ends, with a compressive load applied;
(c) Clamped ends, with a shortening displacement applied, and
(d) Clamped ends, with a compressive load applied.

The results in [8] are compared with the results obtained in the present investigation (using linearized buckling analysis) in Table 6.2.3 for the clamped case, and good agreement is obtained. The critical loads for the free end boundary conditions are approximately half of those of the clamped case. The associated mode shape consists of two sine waves in the circumferential direction and none in the axial direction, in agreement with the analytical results of Hoff and Soong [35].

The mode shape predicted by the linearization buckling analysis for the clamped cylinder case under the action of a compressive load is axisymmetric, as shown in Fig. 6.2.4(b). However, when the load–deflection curve was traced and the linearized buckling analysis
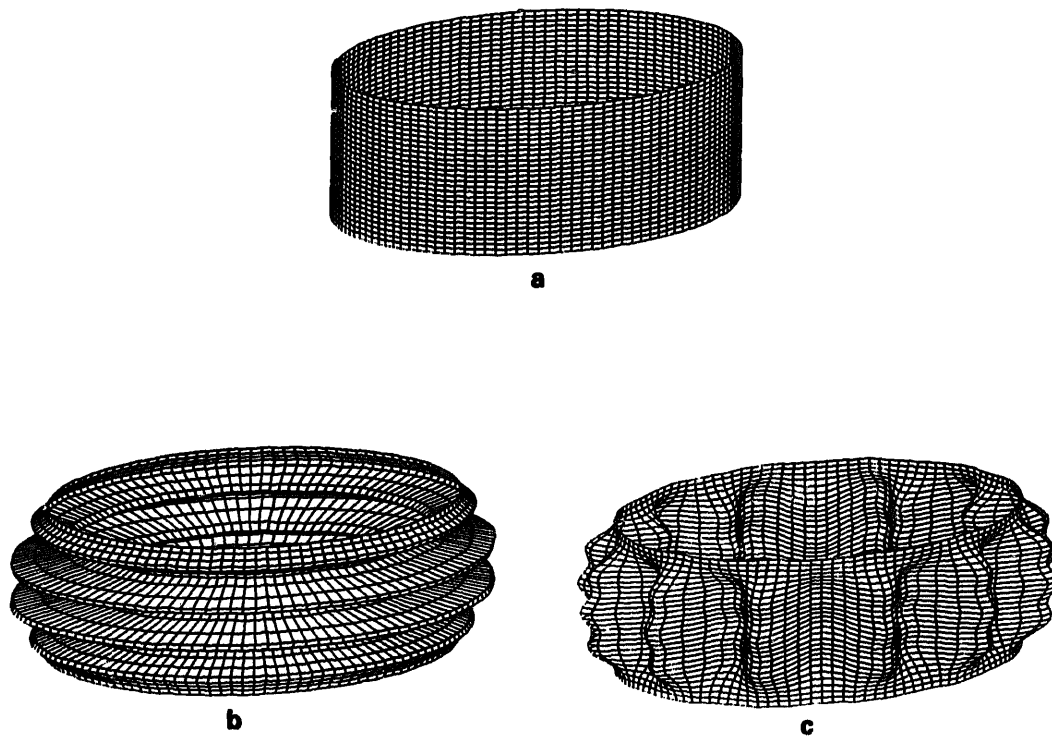
Fig. 6.2.4. (a) Mesh discretization of the buckling of an axially compressed cylinder example. A mesh consisting of 30 elements in the circumferential direction and 14 elements in the axial direction is used to model a one-eighth section of the cylinder using symmetry boundary conditions. This mesh is the same as that used in Liu et al. [8]. (b) Axisymmetric buckling mode resulting from linearized buckling analysis of the axially compressed clamped cylinder. (c) Non-axisymmetric buckling mode produced by performing the buckling analysis at the bifurcation point. The bifurcation point was arrived at by employing an extended system of equations.

Table 6.2.3
Normalized critical load P/P_{cl} for different boundary conditions

Case	4-RSDS	4-SRI	present
(a)	—	—	0.5402
(b)	—	—	0.5055
(c)	1.0369	1.1378	1.0837
(d)	1.0379	1.1361	1.0833

performed in the vicinity of the bifurcation point, the mode predicted was no longer axisymmetric, but reticulated. Figure 6.2.4(c) shows the mode shape associated with the critical load when the linearized buckling analysis is performed at the bifurcation point, where $P/P_{cl} = 1.04$. This example illustrates the important fact that results obtained with a linearized buckling analysis should be interpreted with caution; even in a problem like the one at hand which is known to behave linearly up to a neighborhood of the bifurcation point. We further remark that knowledge of the exact mode shape associated with the lowest buckling load often proves to be crucial for a complete imperfection–sensitivity analysis of a thin shell. Such an analysis is often carried out by adding a scaled mode shape as initial imperfection to the reference configuration. The resulting reduction factor on the buckling load is, of course, highly dependent on the shape of the added imperfection. This is illustrated in Section 6.3.3 where the numerical simulations presented exhibit the strong dependence of the post-buckling response of the cylinder, not only on the level of the added imperfection, but also on slight differences in its shape.

6.3. Snap-through and post-buckling analysis

Our last set of numerical simulations is concerned with the accurate representation of the post-buckling/post-limit response of thin-shells. Our solution procedure for tracing the non-linear load–deflection paths in the post-critical range makes essential use of standard continuation techniques as in [21, 36, 37] and others. In particular, we employ an arc-length constraint in the form of updated hyperplane arc-length. Our implementation is essentially that described in [32, 38].

6.3.1. Snap-through of a hinged cylindrical panel

A shallow shell in the form of a cylindrical panel with small curvature is pinned and subjected to a central load, as shown in Fig. 6.3.1. Increasing values of the applied load lead, eventually, to snap-through of the panel and reversal of its curvature. This problem is simulated using a 4×4 mesh on one quadrant using symmetry conditions for two different thickness: $R/t = 200$, (Fig. 6.31(a)) and $R/t = 400$ (Fig. 6.3.1(b)). In the case of $R/t = 200$, the load–deflection path contains two limit points, and displacement control can be used to solve the equations successfully. In the $R/t = 400$ case, however, the path 'kicks in' after the first limit-point, displacement-control thus fails and use of arc-length control becomes necessary. The results shown in Figs. 6.3.1(a, b), obtained with rather large load steps, are in complete agreement with those reported in the literature; see, i.e., [39, 40].

6.3.2. Buckling of a clamped L-shaped plate under an in-plane bending load

The 68 element mesh for the problem described in section 6.2.2 is used to evaluate the post-buckling response of the square bracket frame. The bifurcation point is arrived at by
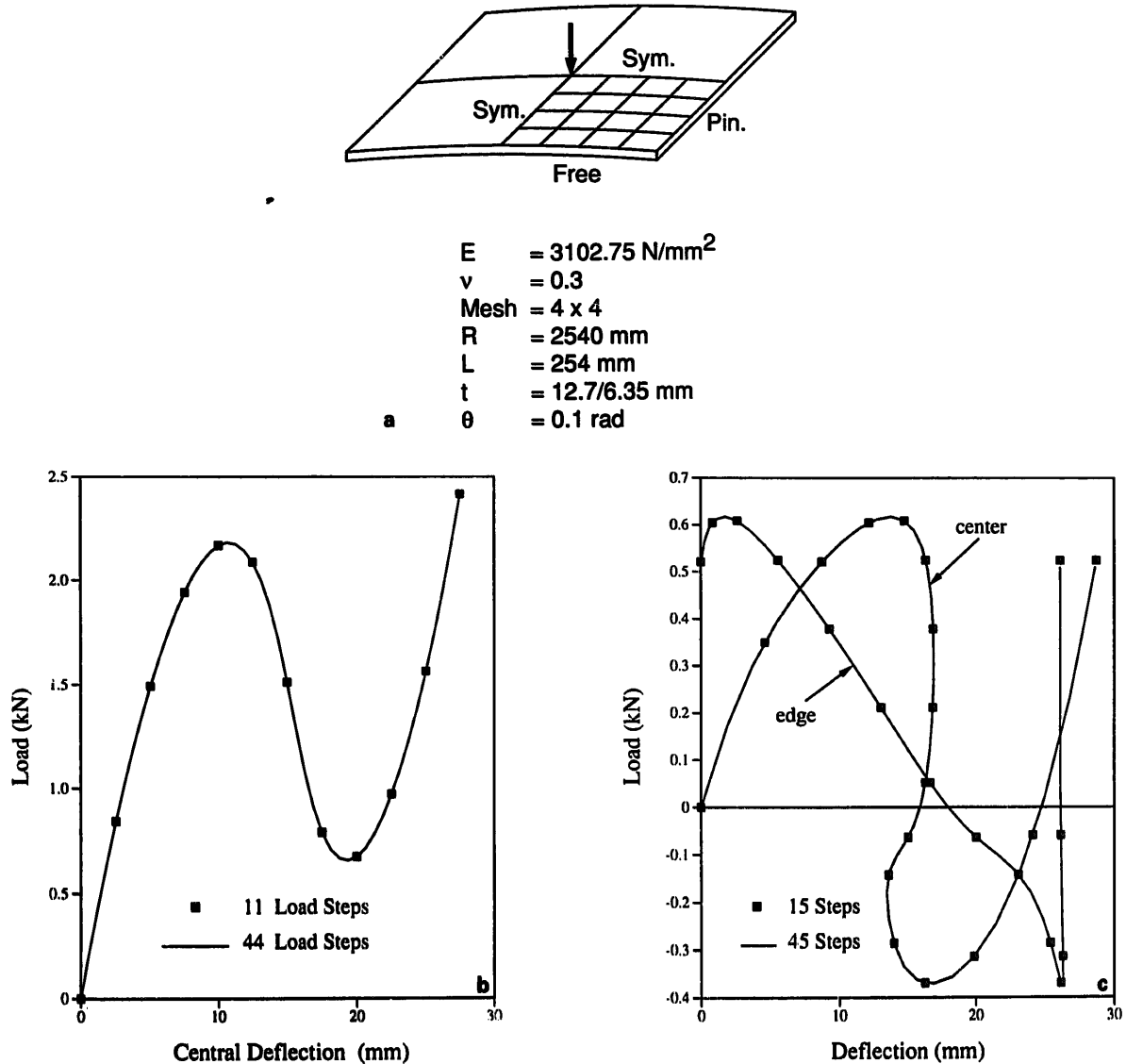
Fig. 6.3.1. (a) Problem definition of the snap-through of a shallow hinged cylindrical panel. A 4 × 4 mesh is used to discretize a quarter-section of the problem, employing symmetry boundary conditions. Two cases are considered by varying the thickness: $R/t = 200$ and $R/t = 400$. (b) Load–deflection path for the $R/t = 200$ case. Displacement control using two different step levels are employed to demonstrate the robustness of the formulation. (c) Load–deflection path for the $R/t = 400$ case. Arc-length control was necessary in this case, due to the limit points and 'kick-ins' present in the solution path. Again two different arc-length levels are employed to demonstrate the robustness of the formulation.

employing an extended system of equations, as described in [30], combined with a mode-switching technique at the bifurcation point, as in [41]. Thus, the stability analysis is performed with no added initial imperfection to the structure. The post-buckling response is shown in Fig. 6.3.2 where a plot of the load versus the deflection in the out-of-plane direction is given. We observe that this load–deflection curve remains flat within a wide range of out-of-plane deflections, up to a value of $\delta z \approx 50$ where a pronounced stiffening of the curve is observed. These results are in good agreement with the general response pattern reported in [16, 31].
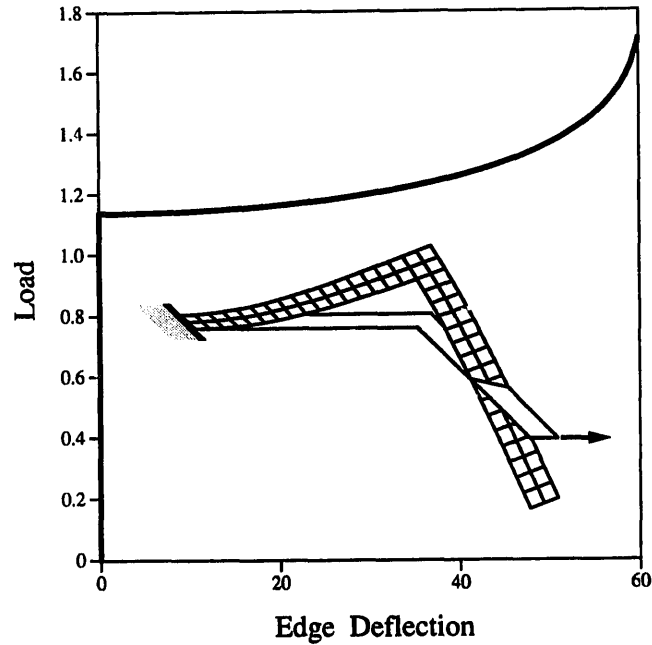
Fig. 6.3.2. Load–deflection curve in the post-buckling regime for the clamped square bracket using a 68 element mesh. The applied load is plotted against the out-of-plane deflection.

6.3.3. Collapse of a rubber sphere

The collapse of a clamped spherical shell of a rubber material (racket ball), is analyzed by Taber [42], both experimentally and analytically, with a theory that includes non-linear edge effects. This theory, however, does not account for shear deformation. The material properties for this problem are $E = 4000$ kPa and $v = 0.5$, the sphere radius is $R = 26.3$ mm and the thickness is $t = 4.4$ mm. The spherical shell (Fig. 6.3.3(a)) is analyzed using one quadrant, symmetry boundary conditions and a 16×16 finite element mesh. The analysis is carried out without shear deformation as in the theory of Taber [42][2]. This is accomplished by a penalty procedure in which the shear coefficient is increased by a factor of 100. The computed load–deflection curve is shown in Fig. 6.3.3(b) along with experimental and analytical results. The excellent agreement found between experimental and computed results is noted. Also shown in Fig. 6.3.3(b) is the sectional deformed shape of the sphere at collapse load.

6.3.4. Post-buckling analysis of a simply-supported cylinder; effect of initial imperfections

A simply-supported cylinder of radius $R = 36$, length $L = 100$, thickness $t = 0.125$ and material properties $E = 10 \times 10^6$ and $v = 0.3$ is subject to a compressive axial load. The objective of the simulation is to trace the load–deflection path in the post-buckling regime and to examine the effect of initial imperfections on the shape of the path. In particular, we are interested in the path corresponding to the buckling-mode consisting of 12 half-sine waves in

---

[2] The values given by Taber [42] for E and v 'compensate' for ignoring the effect of a transverse shear deformation. If shear deformation is taken into account, the computed results are below the curve in Fig. 6.3.3 and agree with recent analytical results of Steele [44] which account for transverse shear deformation.
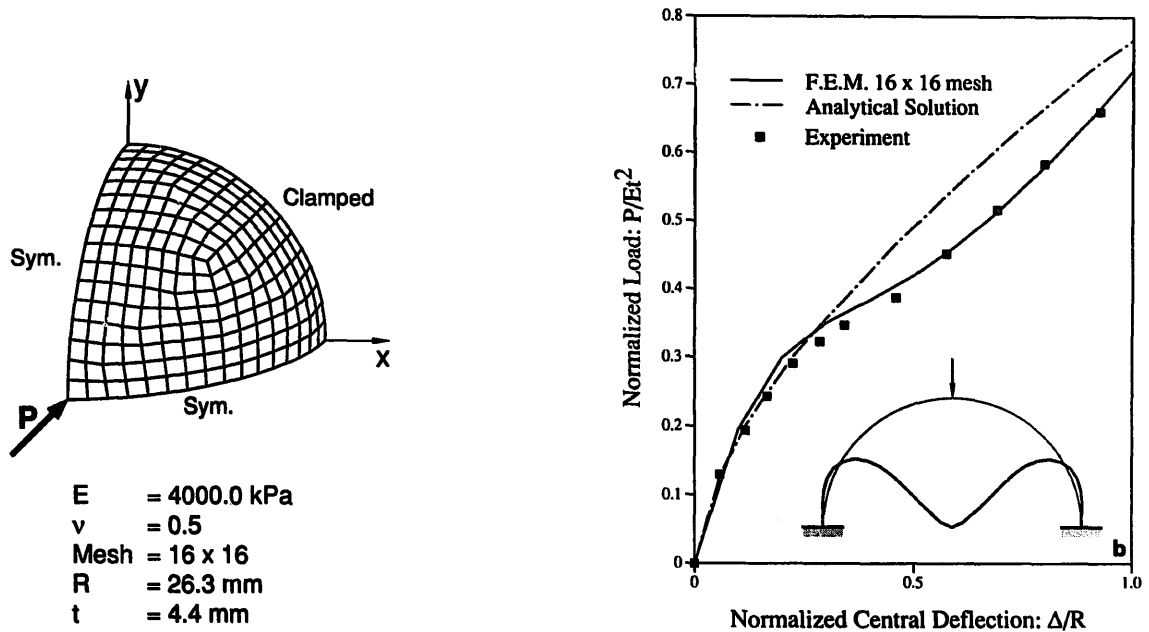
Fig. 6.3.3. (a) Problem definition for the collapse of a rubber sphere example. A 16 × 16 mesh is used to discretize a quarter of the hemisphere, which is clamped at the bottom and pinched at the top until collapse. The material properties were obtained experimentally by Taber [42]. (b) The normalized load–deflection response curve of the collapse of a rubber sphere example. The deflections are normalized with respect to the initial radius, and the calculation is performed in ten displacement steps until complete collapse of the sphere (i.e., $\Delta = R$) was obtained. The initial and deformed sections are shown in the inset. Also shown are the analytical and experimental results of Taber [42].

the circumferential direction and 5 half-sine waves in the axial direction (diamond mode). To this end, as in Stanley [7], we model an $L/10 \times 15°$ section of the cylinder using symmetry boundary conditions on the vertical and interior edges and a simply-supported condition on the loaded edge. A 10×10 mesh is used for this simulation. This problem has been analytically investigated using moderate rotation shell theory by Donnell and Wan [43]. Stanley [7] presents the results of both the 9-ANS and STAGS-C1 degenerated solid elements.

Figure 6.3.4(a) shows the applied load versus the computed maximum axial deflection, for levels of 10% and 50% thickness imperfection with shape corresponding to the lowest linearized buckling mode. Also shown in this figure are the results of Stanley [7]. Excellent agreement is found between both formulations. These results illustrate the importance of the level of imperfections on the post-buckling response.

Figure 6.3.4(b), on the other hand, shows the applied load versus the computed maximum axial deflection for the same levels of imperfection; i.e., 10% and 50% of the thickness, but with different imperfection shapes. The solid line corresponds to an imperfection added to the reference configuration in the shape of the lowest linearized buckling mode, whereas the dash–dot line corresponds to an imperfection in the shape of the lowest buckling mode computed at the bifurcation point. The striking differences between these two results (they correspond essentially to the same mode but they are computed at different points) under-score the importance of performing the eigenvalue analysis at the bifurcation point.

Figure 6.3.4(c) depicts the load–deflection curves with the axial deflection shown in terms of
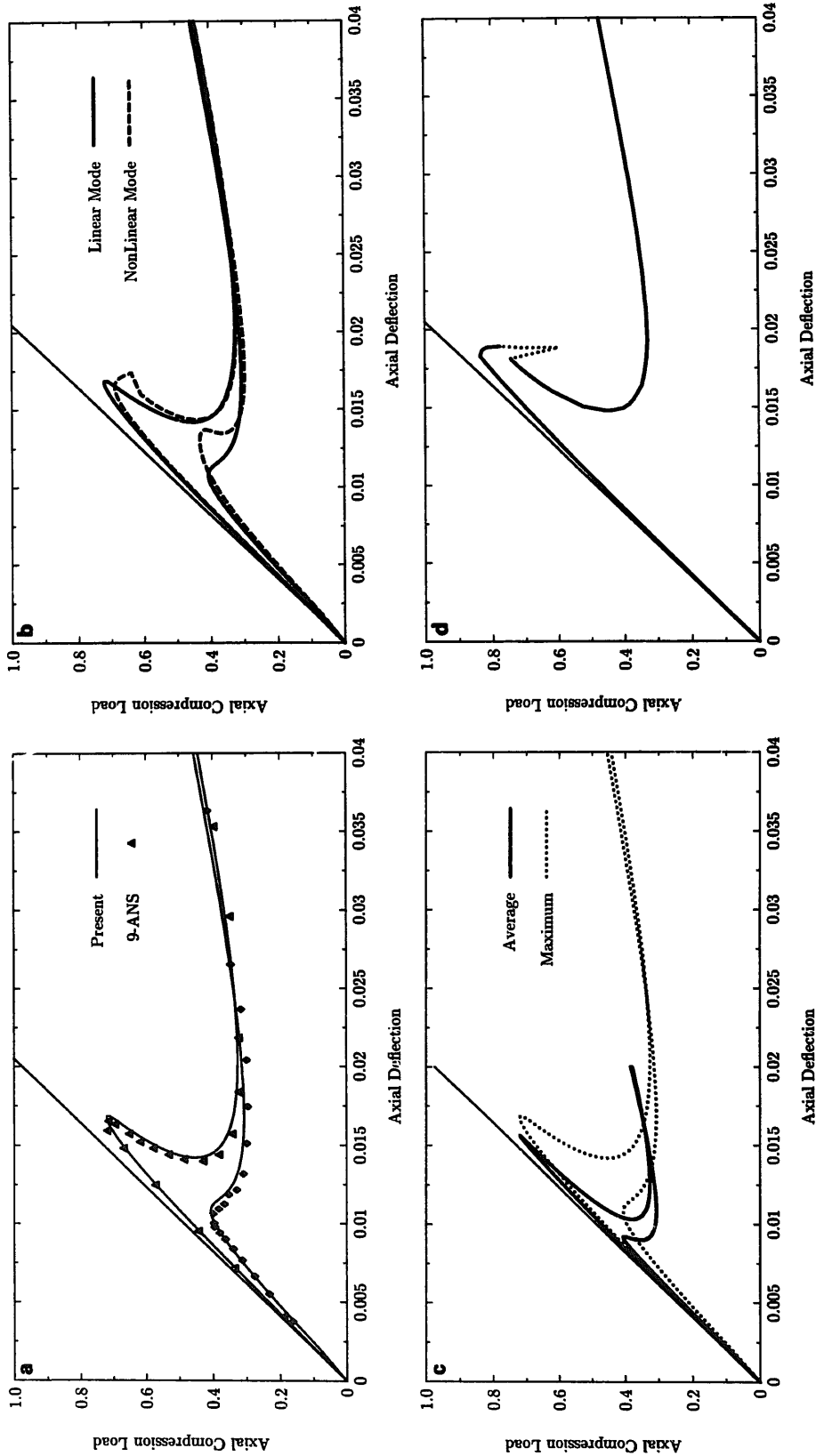
Fig. 6.3.4. (a) Applied load versus the maximum axial deflection at the simply-supported edge for the post-buckling regime of the axially compressed cylinder. The results are shown for two different levels of imperfections ($10\% \times$ and $50\% \times$ thickness) in the shape of the linear mode obtained using linearized buckling analysis. Also shown are the results of Stanley [7]. Results are normalized with the linear buckling load. (b) Comparison of the post-buckling response of the simply-supported axially compressed cylinder using different imperfection shapes. The modes obtained using linearized buckling analysis and non-linear buckling analysis, are added to the initial configuration in levels of $10\% \times$ and $50\% \times$ thickness. The striking differences between the curves underscore the sensitivity of the post-buckling response to the shape as well as to the level of imperfection. Results are normalized with the linear buckling load. (c) Post-buckling response of the simply-supported cylinder in terms of applied load versus maximum axial displacement and average axial displacement at the simply-supported edge, respectively. The striking differences are due to the non-axisymmetry of the buckling modes. Results are normalized with the linear buckling load. (d) Post-buckling response of a perfect axially compressed simply-supported cylinder. The calculation is performed using mode superposition techniques at the bifurcation point. Due to the presence of a multiplicity of clustered modes in the immediate vicinity of the bifurcation point, severe difficulties are experienced by the arc-length method. These difficulties are also noted by Stanley [7], even with a $1\% \times$ thickness imperfection added. Results are normalized with the linear buckling mode.

average axial displacement (solid lines) and maximum axial displacement (dotted lines). Due to the non-axisymmetry of the reticulated buckling mode, the important differences in the magnitudes of the maximum and average axial displacements should be noted.

Figure 6.3.4(d) shows the applied load versus maximum axial displacement curve in the post-buckling range obtained with no added imperfection, computed by means of a branch-switching technique. Two points are worth emphasizing. (i) The difficulties involved in obtaining the curve. Essentially, a multiplicity of clustered critical points are found in the vicinity of the first bifurcation point. One has to carefully monitor the arc-length constraint for the solution procedure not to blow-up. (ii) The shape of the curve (more precisely of the envelope curve since the solution process often changes paths) closely resembles that obtained with a small level initial imperfection in the shape of the lowest buckling mode at the bifurcation point. Finally, the good agreement between the computed results and the classical observations on the post-buckling of thin cylinders, as reported in [43] or [33], is noted.

6.4. Convergence results for the Newton iterations

Since we have at our disposal the exact closed-form expression for the tangent operator, a classical Newton method solution procedure exhibits asymptotically a quadratic rate of convergence. This rate was observed in all the problems examined. As an illustration, we record in Tables 6.4.1 and 6.4.2 the values of the Euclidean norm of the residual, and the energy norm obtained during the first load step in Examples 6.1.2 and 6.3.1. In addition, analogous results are reported in Table 6.4.3 for Example 6.3.3 when only a single load step is employed to attain full collapse of the sphere. These results clearly exhibit the quadratic rate of asymptotic convergence to be expected when the exact Jacobian matrix is employed.

Table 6.4.1
Convergence results for Example 6.1.2; in-plane buckling of a clamped beam

Iteration	Residual norm	Energy norm
0	$0.1414 \times 10^{+01}$	1.6064×10^{-01}
1	$0.2949 \times 10^{+03}$	5.9816×10^{-01}
2	$0.2660 \times 10^{+01}$	0.4978×10^{-04}
3	0.5043×10^{-03}	0.4558×10^{-09}
4	0.8652×10^{-06}	0.5307×10^{-17}
5	0.2655×10^{-11}	0.9956×10^{-28}

Table 6.4.2
Convergence results for Example 6.3.1; snap-through of a hinged cylindrical panel

Iteration	Residual norm	Energy norm
0	$0.1149 \times 10^{+7}$	$0.1356 \times 10^{+06}$
1	$0.9602 \times 10^{+3}$	$0.1567 \times 10^{+01}$
2	$0.2015 \times 10^{+1}$	0.1068×10^{-03}
3	0.1053×10^{-3}	0.3867×10^{-12}
4	0.6726×10^{-6}	0.5224×10^{-19}

Table 6.4.3
Convergence results for Example 6.3.3; collapse of a rubber
sphere in one load step

Iteration	Residual norm	Energy norm
0	$0.1029 \times 10^{+6}$	$0.1585 \times 10^{+07}$
1	$0.4518 \times 10^{+6}$	$0.4317 \times 10^{+07}$
2	$0.1356 \times 10^{+6}$	$0.7294 \times 10^{+06}$
3	$0.3856 \times 10^{+5}$	$0.1171 \times 10^{+06}$
4	$0.1061 \times 10^{+5}$	$0.1968 \times 10^{+05}$
5	$0.3181 \times 10^{+4}$	$0.2080 \times 10^{+04}$
6	$0.5074 \times 10^{+3}$	$0.4784 \times 10^{+02}$
7	$0.1662 \times 10^{+2}$	0.4265×10^{-01}
8	0.2742×10^{-1}	0.7316×10^{-07}
9	0.6215×10^{-7}	0.6216×10^{-18}

7. Closure

In this paper, we have presented a detailed analysis of the computational aspects involved in the finite element implementation of the geometrically exact, stress resultant shell model developed in Part I. By exploiting the geometric structure of the model we are able to develop update procedures for the director field which are exact and singularity-free regardless the magnitude of the incremental director displacement. We have also extended to the fully nonlinear regime the finite element interpolations developed in Part II.

We have illustrated our formulation with a fairly comprehensive set of numerical simulations. An effort has been made to document as completely as possible these simulations to promote further comparisons with the work of other investigators. In the same vein, in Appendix C we have included a rather complete step-by-step description of the finite element implementation.

Acknowledgment

Appendix A. Discrete weak form of the equilibrium equations

Using the following interpolations:

$$\delta\varphi^k = \sum_{A=1}^{4} N^A(\xi, \eta)\delta\varphi_A^k \quad \text{and} \quad \delta t^k = \sum_{A=1}^{4} N^A(\xi, \eta)\delta t_A^k, \tag{A.1}$$

and the assumed strain interpolation for the shear strains (as discussed in Section 6 of Part II), the weak form of the momentum balance equations becomes

$$\bar{G}(\Phi^k; \delta\Phi^k) = \sum_{A=1}^{4} \int_{\mathscr{A}} \{ [B_m^A \delta\varphi_A^k]^t \tilde{n} + [B_{sm}(\delta\varphi^k) + B_{sb}(\delta T^k)]^t \tilde{q}$$

$$+ [B_{bm}^A \delta\varphi_A^k + B_{bb}^A \delta T_A^k]^t \tilde{m} \} \, d\mu^0 - G_{ext}(\delta\Phi^k) \, . \tag{A.2}$$

Here, the definitions of $\tilde{n}$, $\tilde{q}$ and $\tilde{m}$ are as given in Box 1 and

$$B_m^A = \begin{bmatrix} N_{,1}^A \varphi_{,1}^t \\ N_{,2}^A \varphi_{,2}^t \\ N_{,2}^A \varphi_{,1}^t + N_{,1}^A \varphi_{,2}^t \end{bmatrix}_{3\times 3} , \tag{A.3}$$

$$B_{bm}^A = \begin{bmatrix} N_{,1}^A t_{,1}^t \\ N_{,2}^A t_{,2}^t \\ N_{,2}^A t_{,1}^t + N_{,1}^A t_{,2}^t \end{bmatrix}_{3\times 3} , \qquad B_{bb}^A = B_m^A \bar{\Lambda}_{A3\times 2} , \tag{A.4}$$

where $\bar{\Lambda}_A$ is a 3×2 transformation matrix. Define

$$(\delta\varphi^k) = \begin{bmatrix} \delta\varphi_1^k \\ \delta\varphi_2^k \\ \delta\varphi_3^k \\ \delta\varphi_4^k \end{bmatrix} \quad \text{and} \quad (\delta T^k) = \begin{bmatrix} \delta T_1^k \\ \delta T_2^k \\ \delta T_3^k \\ \delta T_4^k \end{bmatrix} . \tag{A.5}$$

Then

$$B_{sm} = \frac{1}{4} \begin{bmatrix} -(1-\eta)t^{B^t} & (1-\eta)t^{B^t} & (1+\eta)t^{D^t} & -(1+\eta)t^{D^t} \\ -(1-\xi)t^{A^t} & -(1+\xi)t^{C^t} & (1+\xi)t^{C^t} & (1-\xi)t^{A^t} \end{bmatrix} , \tag{A.6}$$

$$B_{sb} = \frac{1}{4} \begin{bmatrix} (1-\eta)\varphi_{,1}^{B^t}\bar{\Lambda}_1 & (1-\eta)\varphi_{,1}^{B^t}\bar{\Lambda}_2 & (1+\eta)\varphi_{,1}^{D^t}\bar{\Lambda}_3 & (1+\eta)\varphi_{,1}^{D^t}\bar{\Lambda}_4 \\ (1-\xi)\varphi_{,2}^{A^t}\bar{\Lambda}_1 & (1+\xi)\varphi_{,2}^{C^t}\bar{\Lambda}_2 & (1+\xi)\varphi_{,2}^{C^t}\bar{\Lambda}_3 & (1-\xi)\varphi_{,2}^{A^t}\bar{\Lambda}_4 \end{bmatrix} , \tag{A.7}$$

where $\{A, B, C, D\}$ refer to the mid-side points of the bilinear element.

Appendix B. The second variation of the strain measures

The linearized strain measures in (5.2) are

$$\delta\varepsilon_{\alpha\beta} = \tfrac{1}{2}(\varphi_{,\alpha} \cdot \delta\varphi_{,\beta} + \delta\varphi_{,\alpha} \cdot \varphi_{,\beta}) \, , \tag{B.1a}$$

$$\delta\gamma_\alpha = \delta\varphi_{,\alpha} \cdot t + \varphi_{,\alpha} \cdot \delta t \, , \tag{B.1b}$$

$$\delta\kappa_{\alpha\beta} = \delta\varphi_{,\alpha} \cdot t_{,\beta} + \varphi_{,\alpha} \cdot \delta t_{,\beta} \, . \tag{B.1c}$$

Following the procedure outlined in Section 2.1.3, the linearization of (B.1) is performed with the aid of the directional derivative. In order to demonstrate the nature of the linearization process, we perform the computation of the term $D(\delta\kappa_{\alpha\beta}) \cdot \Delta\Phi =: \Delta(\delta\kappa_{\alpha\beta})$, where the notation of (5.9) is used. Introducing the interpolations (4.2) and (4.8) into (B.1c), we have

$$\delta\kappa_{\alpha\beta} = \sum_{A=1}^{4} N_{,\alpha}^{A}\, \delta\varphi_{A} \cdot t_{,\beta} + \varphi_{,\alpha} \cdot \sum_{A=1}^{4} N_{,\beta}^{A}\, \delta t_{A} \,. \tag{B.2}$$

By making use of definition (5.9) on (B.2), we obtain

$$\Delta(\delta\kappa_{\alpha\beta}) = \frac{d}{d\varepsilon}\Big|_{\varepsilon=0} \Big\{ \sum_{A=1}^{4} N_{,\alpha}^{A}\, \delta\varphi_{A} \cdot t_{\varepsilon,\beta} + \varphi_{\varepsilon,\alpha} \cdot \sum_{A=1}^{4} N_{,\beta}^{A}(\delta t_{A})_{\varepsilon} \Big\} \,. \tag{B.3}$$

Recall from Section 2.1.3 that $\varphi_{\varepsilon} = \varphi + \varepsilon\Delta\varphi$, $t_{\varepsilon} = \exp[\varepsilon\widehat{\Delta\theta}]t$ and $(\delta t_{A})_{\varepsilon} = \delta\theta_{A} \times t_{A\varepsilon}$. Equation (B.3) then becomes

$$\Delta(\delta\kappa_{\alpha\beta}) = \sum_{A=1}^{4} N_{,\alpha}^{A}\, \delta\varphi_{A} \cdot (\Delta\theta \times t)_{,\beta} + \Delta\varphi_{,\alpha} \cdot \sum_{A=1}^{4} N_{,\beta}^{A}\, \delta t_{A}$$

$$+ \varphi_{,\alpha} \cdot \sum_{A=1}^{4} N_{,\beta}^{A}(\delta\theta_{A} \times [\Delta\theta_{A} \times t_{A}]) \,. \tag{B.4}$$

Again, introducing interpolations (4.2) and (4.8), we obtain

$$\Delta(\delta\kappa_{\alpha\beta}) = \sum_{A=1}^{4}\sum_{B=1}^{4} \{N_{,\alpha}^{A}N_{,\beta}^{B}\, \delta\varphi_{A}^{t}\, \Delta t_{B} + N_{,\alpha}^{B}\, N_{,\beta}^{A}\, \Delta\varphi_{B}^{t}\, \delta t_{A}\}$$

$$- \varphi_{,\alpha} \cdot \sum_{A=1}^{4} N_{,\beta}^{A}(\delta t_{A} \cdot \Delta t_{A})t_{A} \,. \tag{B.5}$$

Similarly, the second variation of the membrane strain is given by

$$\Delta(\delta\varepsilon_{\alpha\beta}) = \frac{1}{2}\Big[\sum_{A=1}^{4}\sum_{B=1}^{4} (N_{,\alpha}^{A}N_{,\beta}^{B} + N_{,\beta}^{A}N_{,\alpha}^{B})\, \delta\varphi_{A}^{t}\, \Delta\varphi_{B} \Big] \,. \tag{B.6}$$

In contrast to the calculation of (B.5) and (B.6), the second variation of the transverse shear strain measure does not follow directly from (B.1b). $\Delta(\delta\gamma_{\alpha})$ is calculated by linearizing the assumed shear strain interpolation presented in Part II. The mechanics of this calculation are identical to the procedure outlined above and the resulting expression is recorded:

$$\begin{bmatrix} \Delta(\delta\gamma_{1}) \\ \Delta(\delta\gamma_{2}) \end{bmatrix} = \frac{1}{8} \begin{bmatrix} (1-\eta)[(\delta\varphi_{2} - \delta\varphi_{1}) \cdot (\Delta t_{1} + \Delta t_{2}) + (\delta t_{1} + \delta t_{2}) \cdot (\Delta\varphi_{2} - \Delta\varphi_{1})] \\ + (1+\eta)[(\delta\varphi_{3} - \delta\varphi_{4}) \cdot (\Delta t_{3} + \Delta t_{4}) + (\delta t_{3} + \delta t_{4}) \cdot (\Delta\varphi_{3} - \Delta\varphi_{4})] \\ (1-\xi)[(\delta\varphi_{4} - \delta\varphi_{1}) \cdot (\Delta t_{1} + \Delta t_{4}) + (\delta t_{1} + \delta t_{4}) \cdot (\Delta\varphi_{4} - \Delta\varphi_{1})] \\ + (1+\xi)[(\delta\varphi_{3} - \delta\varphi_{2}) \cdot (\Delta t_{2} + \Delta t_{3}) + (\delta t_{2} + \delta t_{3}) \cdot (\Delta\varphi_{3} - \Delta\varphi_{2})] \end{bmatrix}$$

$$- \frac{1}{4} \begin{bmatrix} (1-\eta)[(^2\varphi_{,1} \cdot t_1)(\delta t_1 \cdot \Delta t_1) + (^2\varphi_{,1} \cdot t_2)(\delta t_2 \cdot \Delta t_2)] \\ + (1+\eta)[(^4\varphi_{,1} \cdot t_3)(\delta t_3 \cdot \Delta t_3) + (^4\varphi_{,1} \cdot t_4)(\delta t_4 \cdot \Delta t_4)] \\ (1-\xi)[(^1\varphi_{,2} \cdot t_1)(\delta t_1 \cdot \Delta t_1) + (^1\varphi_{,2} \cdot t_4)(\delta t_4 \cdot \Delta t_4)] \\ + (1+\xi)[(^3\varphi_{,2} \cdot t_2)(\delta t_2 \cdot \Delta t_2) + (^3\varphi_{,2} \cdot t_3)(\delta t_3 \cdot \Delta t_3)] \end{bmatrix} . \tag{B.7}$$

Appendix C. Implementation notes

In this section, a detailed description of the implementation of the proposed shell model, including explicit expressions for the tangent matrices, is presented. This flowchart-like account is presented in two sections: the initial calculations to be performed at the reference configuration, and the updates and stiffness calculations to be performed at the current configuration. A list of the notation employed in this section is found in Table C.1. To alleviate the notation, the h superscripts will be omitted throughout.

C.1. Reference configuration

C.1.1. Interpolate directors

(i) Gauss points and assumed strain points.

$$t_e^{(0)} = \frac{\tilde{t}_e^{(0)}}{\|\tilde{t}_e^{(0)}\|} , \qquad \tilde{t}_e^{(0)} := \sum_{I=1}^{4} N^I t_I^{(0)} .$$

(ii) Gauss point director derivatives.

$$\mathbb{P}_t^{(0)} := \mathbf{1}_3 - t_e^{(0)} \otimes t_e^{(0)} , \qquad \tilde{t}_{,\alpha}^{(0)} := \sum_{I=1}^{4} N^I_{,\alpha} t_I^{(0)} , \qquad t_{,\alpha}^{(0)} = \frac{1}{\|\tilde{t}_e^{(0)}\|} \mathbb{P}_t^{(0)} \tilde{t}_{,\alpha}^{(0)} \quad (\alpha = 1,2) .$$

Table C.1
Notation

Subscripts and superscripts	
$I = 1, 2, 3, 4$	Element nodal points,
$G = 1, 2, 3, 4$	Full quadrature integration points,
$M = A, B, C, D$	Assumed-strain mid-side points,
O	Element centroid,
(0)	Reference configuration,
(k)	Iteration k, current configuration.

Global data	
t_I	Nodal directors,
x_I	Nodal position vectors,
u_I	Total displacement vectors,
ΔT_I	Incremental rotation vectors.

(iii) Rotational transformation matrices at nodal and assumed strain points.[3]

$$\bar{A}_I^{(0)} = \text{first two columns of } A_I^{(0)} = [t_1^{(0)}|t_2^{(0)}|t^{(0)}]_I ,$$

$$A_I^{(0)} = (E \cdot t_I^{(0)})1_3 + [\widehat{E \times t_I^{(0)}}] + \frac{(E \times t_I^{(0)}) \otimes (E \times t_I^{(0)})}{1 + E \cdot t_I^{(0)}} .$$

C.1.2. Construct cartesian frames
(i) Centroidal normal.

$$\varphi_{O,\alpha}^{(0)} = \sum_{I=1}^{4} N_{,\alpha}^I|_{\xi=\eta=0} x_I \quad (\alpha = 1,2), \qquad \nu_O^{(0)} := \frac{\varphi_{O,1}^{(0)} \times \varphi_{O,2}^{(0)}}{\|\varphi_{O,1}^{(0)} \times \varphi_{O,2}^{(0)}\|} .$$

(ii) Gauss point normals.

$$\varphi_{G,\alpha}^{(0)} = \sum_{I=1}^{4} N_{,\alpha}^I|_{\xi_G,\eta_G} x_I \quad (\alpha = 1,2), \qquad \nu_G^{(0)} := \frac{\varphi_{G,1}^{(0)} \times \varphi_{G,2}^{(0)}}{\|\varphi_{G,1}^{(0)} \times \varphi_{G,2}^{(0)}\|} .$$

(iii) Rotational transformation matrices.

$$\bar{A}^{(0)} = \text{first two columns of } A^{(0)} = [\nu_1^{(0)} \mid \nu_2^{(0)} \mid \nu^{(0)}] ,$$

$$A_G^{(0)} = (E \cdot \nu_G^{(0)})1_3 + [\widehat{E \times \nu_G^{(0)}}] + \frac{(E \times \nu_G^{(0)}) \otimes (E \times \nu_G^{(0)})}{1 + E \cdot \nu_G^{(0)}} ,$$

$$A_O^{(0)} = (E \cdot \nu_O^{(0)})1_3 + [\widehat{E \times \nu_O^{(0)}}] + \frac{(E \times \nu_O^{(0)}) \otimes (E \times \nu_O^{(0)})}{1 + E \cdot \nu_O^{(0)}} ,$$

(iv) Jacobian transformation matrices.

$$J_G^{(0)} = \begin{bmatrix} \nu_{G_1}^{(0)} \cdot \varphi_{G,1}^{(0)} & \nu_{G_1}^{(0)} \cdot \varphi_{G,2}^{(0)} \\ \nu_{G_2}^{(0)} \cdot \varphi_{G,1}^{(0)} & \nu_{G_2}^{(0)} \cdot \varphi_{G,2}^{(0)} \end{bmatrix}, \qquad J_O^{(0)} = \begin{bmatrix} \nu_{O_1}^{(0)} \cdot \varphi_{O,1}^{(0)} & \nu_{O_1}^{(0)} \cdot \varphi_{O,2}^{(0)} \\ \nu_{O_2}^{(0)} \cdot \varphi_{O,1}^{(0)} & \nu_{O_2}^{(0)} \cdot \varphi_{O,2}^{(0)} \end{bmatrix} .$$

(v) Cartesian shape function derivatives at Gauss points.

$$\begin{bmatrix} \tilde{N}_{,1}^I \\ \tilde{N}_{,2}^I \end{bmatrix} = J_G^{(0)-t} \begin{bmatrix} N_{,\xi}^I \\ N_{,\eta}^I \end{bmatrix} .$$

---

[3] The expression used here for the initial transformation matrices is not an essential requirement, but rather a convenient way of setting up a Cartesian system about the directors. It may be substituted for by any other set of orthonormal vectors normal to the directors. In fact, these systems may even be selected in the mesh generation, in order to accommodate special boundary conditions.

C.1.3. Initial strain measures

(i) Reference Jacobian.

$$\bar{j}_G^{(0)} = \|\varphi_{G,1}^{(0)} \times \varphi_{G,2}^{(0)}\| .$$

(ii) Reference metric tensor.

$$a_{\alpha\beta}^{(0)} = \varphi_{G,\alpha}^{(0)} \cdot \varphi_{G,\beta}^{(0)} , \qquad [a^{(0)\alpha\beta}] = [a_{\alpha\beta}^{(0)}]^{-1} .$$

(iii) Transverse shear strain measures.

$$\varphi_{A,2}^{(0)} = \tfrac{1}{2}(x_4 - x_1) , \qquad \varphi_{B,1}^{(0)} = \tfrac{1}{2}(x_2 - x_1) ,$$

$$\varphi_{C,2}^{(0)} = \tfrac{1}{2}(x_3 - x_2) , \qquad \varphi_{D,1}^{(0)} = \tfrac{1}{2}(x_3 - x_4) ,$$

$$\gamma_G^{(0)} = \frac{1}{2} \begin{bmatrix} (1-\eta)\varphi_{B,1}^{(0)} \cdot t_B^{(0)} + (1+\eta)\varphi_{D,1}^{(0)} \cdot t_D^{(0)} \\ (1-\xi)\varphi_{A,2}^{(0)} \cdot t_A^{(0)} + (1+\xi)\varphi_{C,2}^{(0)} \cdot t_C^{(0)} \end{bmatrix} .$$

(iv) Reference curvatures.

$$\kappa_G^{(0)} = \begin{bmatrix} \varphi_{G,1}^{(0)} \cdot t_{G,1}^{(0)} \\ \varphi_{G,2}^{(0)} \cdot t_{G,2}^{(0)} \\ \varphi_{G,1}^{(0)} \cdot t_{G,2}^{(0)} + \varphi_{G,2}^{(0)} \cdot t_{G,1}^{(0)} \end{bmatrix} .$$

C.2. Current configuration

C.2.1. Update directors

(i) Update of nodal directors and nodal rotation matrices.

$$\underbrace{\Delta t_I^{(k)}}_{(3 \times 1)} = \underbrace{\bar{\Lambda}_I^{(k)}}_{(3 \times 2)} \underbrace{\Delta T_I^{(k)}}_{(2 \times 1)} ,$$

$$t_I^{(k+1)} \leftarrow \cos \| \Delta t_I^{(k)} \| t_I^{(k)} + \frac{\sin \| \Delta t_I^{(k)} \|}{\| \Delta t_I^{(k)} \|} \Delta t_I^{(k)} ,$$

$$\Delta\theta := t_I^{(k)} \times \Delta t_I^{(k)} ,$$

$$\Delta\Lambda_I^{(k)} = \cos \| \Delta t_I^{(k)} \| 1_3 + \frac{\sin \| \Delta t_I^{(k)} \|}{\| \Delta t_I^{(k)} \|} [\widehat{\Delta\theta}] + \frac{1 - \cos \| \Delta t_I^{(k)} \|}{\| \Delta t_I^{(k)} \|^2} \Delta\theta \otimes \Delta\theta ,$$

$$\Lambda_I^{(k+1)} \leftarrow \Delta\Lambda_I^{(k)} \Lambda_I^{(k)} .$$

(ii) Update of curvatures at Gauss-points.

$$\Delta t_G^{(k)} = \sum_{I=1}^{4} N_I \Delta t_I^{(k)} ,$$

$$\Delta t_{G,\alpha}^{(k)} = \sum_{I=1}^{4} N_{I,\alpha} \Delta t_I^{(k)} \quad (\alpha = 1, 2) \ ,$$

$$t_G^{(k+1)} \leftarrow \cos \| \Delta t_G^{(k)} \| t_G^{(k)} + \frac{\sin \| \Delta t_G^{(k)} \|}{\| \Delta t_G^{(k)} \|} \Delta t_G^{(k)} \ ,$$

$$T^{(k+1)} = \frac{\sin \| \Delta t_G^{(k)} \|}{\| \Delta t_G^{(k)} \|} [(1_3 - t_G^{(k)}) \otimes \Delta t_G^{(k)}] + \frac{\cos \| \Delta t_G^{(k)} \| - \dfrac{\sin \| \Delta t_G^{(k)} \|}{\| \Delta t_G^{(k)} \|}}{\| \Delta t_G^{(k)} \|^2} \Delta t_G^{(k)} \otimes \Delta t_G^{(k)} \ ,$$

$$t_{G,\alpha}^{(k+1)} \leftarrow \cos \| \Delta t_G^{(k)} \| t_{G,\alpha}^{(k)} + T^{(k+1)} \Delta t_{G,\alpha}^{(k)} \quad (\alpha = 1, 2) \ .$$

(iii) Update of directors at assumed-strain points.

$$\Delta t_A^{(k)} = \tfrac{1}{2} (\Delta t_4^{(k)} + \Delta t_1^{(k)}) \ , \qquad \Delta t_B^{(k)} = \tfrac{1}{2} (\Delta t_1^{(k)} + \Delta t_2^{(k)}) \ ,$$

$$\Delta t_C^{(k)} = \tfrac{1}{2} (\Delta t_2^{(k)} + \Delta t_3^{(k)}) \ , \qquad \Delta t_D^{(k)} = \tfrac{1}{2} (\Delta t_3^{(k)} + \Delta t_4^{(k)}) \ ,$$

$$t_M^{(k+1)} \leftarrow \cos \| \Delta t_M^{(k)} \| t_M^{(k)} + \frac{\sin \| \Delta t_M^{(k)} \|}{\| \Delta t_M^{(k)} \|} \Delta t_M^{(k)} \ .$$

C.2.2. Membrane interpolation; residual and tangent stiffness
(i) Mixed interpolation parameters.

$$\bar{\mathscr{F}}_1 = \begin{bmatrix} (J_{O1}^1)^2 \\ (J_{O1}^2)^2 \\ J_{O1}^1 J_{O1}^2 \end{bmatrix} \ , \qquad \bar{\mathscr{F}}_2 = \begin{bmatrix} (J_{O1}^1)^2 \\ (J_{O2}^2)^2 \\ J_{O2}^1 J_{O2}^2 \end{bmatrix} \ ,$$

$$\bar{\xi} = \frac{1}{\mathscr{A}_e} \int_{\bar{\Omega}} \xi \, \mathrm{d}\mu^0 \ , \qquad \bar{\eta} = \frac{1}{\mathscr{A}_e} \int_{\bar{\Omega}} \eta \, \mathrm{d}\mu^0 \ ,$$

$$S(\xi, \eta) = [1_3 \,|\, (\eta - \bar{\eta}) \bar{\mathscr{F}}_1 (\xi - \bar{\xi}) \bar{\mathscr{F}}_2] \ .$$

(ii) Inverse constitutive matrix (local Cartesian systems).

$$\mathbb{C}_m^{-1} = \frac{1}{Eh} \begin{bmatrix} 1 & -\nu & 0 \\ -\nu & 1 & 0 \\ 0 & 0 & 2(1 + \nu) \end{bmatrix} \ .$$

(iii) Discrete strain–displacement operator.

$$B_m^I = \begin{bmatrix} \tilde{N}_{,1}^I \varphi_{0,1}^{(k+1)^t} \\ \tilde{N}_{,2}^I \varphi_{0,2}^{(k+1)^t} \\ \tilde{N}_{,1}^I \varphi_{0,2}^{(k+1)^t} + \tilde{N}_{,2}^I \varphi_{0,1}^{(k+1)^t} \end{bmatrix} \ .$$

(iv) Mixed form.

$$H_m = \sum_{G=1}^{G-P_{ts}} S_G^t C_m^{-1} S_G \bar{j}_G^0 \mathcal{W}_G \,,$$

$$G_m^I = \sum_{G=1}^{G-P_{ts}} S_G^t B_m^I \bar{j}_G^0 \mathcal{W}_G \,.$$

(v) Membrane strains.

$$\varphi_{G,a}^{(0)} = \sum_{I=1}^{4} \tilde{N}_{,a}^I|_{\xi_G,\eta_G}(x_I + u_I) \quad (a = 1,2) \,,$$

$$a_G = \frac{1}{2} \begin{bmatrix} \varphi_{G,1}^{(0)} \cdot \varphi_{G,1}^{(0)} - 1 \\ \varphi_{G,2}^{(0)} \cdot \varphi_{G,2}^{(0)} - 1 \\ 2\varphi_{G,1}^{(0)} \cdot \varphi_{G,2}^{(0)} \end{bmatrix} \,.$$

(vi) Membrane stresses.

$$\beta_m = \sum_{G=1}^{G-P_{ts}} S_G a_G \bar{j}_G^0 \mathcal{W}_G \,, \qquad n_G = S_G^t H_m^{-1} \beta_m \,.$$

(vii) Membrane contribution to tangent stiffness.

— Material:

$$MK_m^{IJ} = G_m^{I^t} H_m^{-1} G_m^J \,;$$

— Geometric:

$$GK_m^{IJ} = \sum_{G=1}^{G-P_{ts}} \left\{ \begin{bmatrix} \tilde{N}_{G,1}^I \tilde{N}_{G,1}^J \\ \tilde{N}_{G,2}^I \tilde{N}_{G,2}^J \\ \tilde{N}_{G,1}^I \tilde{N}_{G,2}^J + \tilde{N}_{G,2}^I \tilde{N}_{G,1}^J \end{bmatrix} \cdot n_G \right\} 1_3 \bar{j}_G^0 \mathcal{W}_G \,,$$

$$K_m^{IJ} = \begin{bmatrix} MK_m^{IJ} + GK_m^{IJ} & 0_{3\times 2} \\ 0_{3\times 2} & 0_{2\times 2} \end{bmatrix} \,.$$

(viii) Membrane contribution to residual.

$$R_m^I = \begin{bmatrix} G_m^I \beta_m \\ 0_{2\times 1} \end{bmatrix} \,.$$

C.2.3. Transverse shear interpolation; residual and tangent stiffness
(i) Constitutive matrix (curvilinear systems).

$$\mathbb{C}_s = \kappa G_s h \begin{bmatrix} a^{(0)^{11}} & a^{(0)^{12}} \\ a^{(0)^{21}} & a^{(0)^{22}} \end{bmatrix} .$$

(ii) Discrete strain–displacement operator.

$$B_s = \left[\underbrace{\begin{bmatrix} N_{,1}^1 t_B^{(k+1)^t} & N_{,1}^2 \varphi_{B,1}^{(k+1)} \cdot \Lambda_1 \\ N_{,2}^1 t_A^{(k+1)^t} & N_{,2}^4 \varphi_{A,2}^{(k+1)} \cdot \Lambda_1 \end{bmatrix}}_{B_s^1} \,\middle\|\, \underbrace{\begin{bmatrix} N_{,1}^2 t_B^{(k+1)^t} & N_{,1}^2 \varphi_{B,1}^{(k+1)} \cdot \Lambda_2 \\ N_{,2}^2 t_C^{(k+1)^t} & N_{,2}^2 t_{C,2}^{(k+1)} \cdot \Lambda_2 \end{bmatrix}}_{B_s^2} \right.$$

$$\left. \,\middle\|\, \underbrace{\begin{bmatrix} N_{,1}^3 t_D^{(k+1)^t} & N_{,1}^3 \varphi_{D,1}^{(k+1)} \cdot \Lambda_3 \\ N_{,2}^3 t_C^{(k+1)^t} & N_{,2}^3 \varphi_{C,2}^{(k+1)} \cdot \Lambda_3 \end{bmatrix}}_{B_s^3} \,\middle\|\, \underbrace{\begin{bmatrix} N_{,1}^4 t_D^{(k+1)^t} & N_{,1}^3 \varphi_{D,1}^{(k+1)} \cdot \Lambda_4 \\ N_{,2}^4 t_A^{(k+1)^t} & N_{,2}^4 \varphi_{A,2}^{(k+1)} \cdot \Lambda_4 \end{bmatrix}}_{B_s^4} \right] .$$

(iii) Transverse shear strains.

$$\varphi_{A,2}^{(k+1)} = \tfrac{1}{2}[(x_4 + u_4) - (x_1 + u_1)], \qquad \varphi_{B,1}^{(k+1)} = \tfrac{1}{2}[(x_2 + u_2) - (x_1 + u_1)],$$

$$\varphi_{C,2}^{(k+1)} = \tfrac{1}{2}[(x_3 + u_3) - (x_2 + u_2)], \qquad \varphi_{D,1}^{(k+1)} = \tfrac{1}{2}[(x_3 + u_3) - (x_4 + u_4)],$$

$$\gamma_G^{(k+1)} = \frac{1}{2} \begin{bmatrix} (1-\eta)\varphi_{B,1}^{(k+1)} \cdot t_B^{(k+1)} + (1+\eta)\varphi_{D,1}^{(k+1)} \cdot t_D^{(k+1)} \\ (1-\xi)\varphi_{A,2}^{(k+1)} \cdot t_A^{(k+1)} + (1+\xi)\varphi_{C,2}^{(k+1)} \cdot t_C^{(k+1)} \end{bmatrix},$$

$$\Xi_G = \gamma_G^{(k+1)} - \gamma_G^{(0)} .$$

(iv) Transverse shear stresses.

$$q_G = \mathbb{C}_s \Xi_G .$$

(v) Transverse shear contribution to tangent stiffness.
— Material:

$$MK_s^{IJ} = B_s^{I^t} \mathbb{C}_s B_s^J ,$$

— Geometric-rotational:

$$GK_{s\,1}^{11} := [-(1-\eta)q^1 - (1-\xi)q^2]\bar{\Lambda}_1 ,$$

$$GK_{s\,1}^{12} := -(1-\eta)q^1 \bar{\Lambda}_2 ,$$

$$GK_{s\,1}^{13} := 0_{3\times2} ,$$

$$GK_{s\,1}^{14} := -(1-\xi)q^2 \bar{\Lambda}_4 ,$$

$$GK_{s\,1}^{22} := [(1-\eta)q^1 - (1+\xi)q^2]\bar{\Lambda}_2 ,$$

$$GK^{23}_{s\,1} := -(1+\xi)q^2\bar{A}_3 \,,$$

$$GK^{24}_{s\,1} := \mathbf{0}_{3\times2} \,,$$

$$GK^{33}_{s\,1} := [(1+\eta)q^1 + (1+\xi)q^2]\bar{A}_3 \,,$$

$$GK^{34}_{s\,1} := (1+\eta)q^1\bar{A}_4 \,,$$

$$GK^{44}_{s\,1} := [-(1+\eta)q^1 + (1-\xi)q^2]\bar{A}_4 \,,$$

$$GK^{JI}_{s\,1} := -GK^{IJ}_{s\,1} \,.$$

— Geometric–diagonal:

$$GK^{11}_{s\,2} := [(1-\eta)q^1(\varphi_{B,1}\cdot t_A) + (1-\xi)q^2(\varphi_{A,2}\cdot t_A)]\mathbf{1} \,,$$

$$GK^{22}_{s\,2} := [(1-\eta)q^1(\varphi_{B,1}\cdot t_B) + (1+\xi)q^2(\varphi_{C,2}\cdot t_B)]\mathbf{1} \,,$$

$$GK^{33}_{s\,2} := [(1+\eta)q^1(\varphi_{D,1}\cdot t_C) + (1+\xi)q^2(\varphi_{C,2}\cdot t_C)]\mathbf{1} \,,$$

$$GK^{44}_{s\,2} := [(1+\eta)q^1(\varphi_{D,1}\cdot t_D) + (1-\xi)q^2(\varphi_{A,2}\cdot t_D)]\mathbf{1} \,.$$

$$K^{IJ}_b = \sum_{G=1}^{G-P_{ts}} \left\{ MK^{IJ}_s + \begin{bmatrix} \mathbf{0}_{3\times3} & \frac{1}{8}GK^{IJ}_{s\,1} \\ \frac{1}{8}GK^{JI^t}_{s\,1} & -\frac{1}{4}GK^{IJ}_{s\,2} \end{bmatrix} \right\} \bar{j}^0_G \mathscr{W}_G \,.$$

(vi) Transverse shear contribution to residual.

$$R^I_s = \sum_{G=1}^{G-P_{ts}} B^{I^t}_s q_G \bar{j}^0_G \mathscr{W}_G \,.$$

C.2.4. Bending interpolation (displacement model)
(i) Constitutive matrix (curvilinear systems).

$$H^{1111} = a^{(0)11}a^{(0)11} \,,$$

$$H^{1122} = \nu a^{(0)11}a^{(0)22} + (1-\nu)a^{(0)12}a^{(0)12} \,,$$

$$H^{1112} = a^{(0)11}a^{(0)12} \,,$$

$$H^{2222} = a^{(0)22}a^{(0)22} \,,$$

$$H^{2212} = a^{(0)22}a^{(0)12} \,,$$

$$H^{1212} = \tfrac{1}{2}[\nu a^{(0)11}a^{(0)22} + (1-\nu)a^{(0)12}a^{(0)12}] \,,$$

$$\mathbb{C}_b = \frac{Eh^3}{12(1-\nu^2)} \begin{bmatrix} H^{1111} & H^{1122} & H^{1112} \\ & H^{2222} & H^{2212} \\ Sym. & & H^{1212} \end{bmatrix} \,.$$

(ii) Discrete strain–displacement operator.

$$
\boldsymbol{B}^I_{\mathrm{bd}} = \begin{bmatrix} t^{(k+1)^t}_{\mathrm{G},1} N^I_{,1} \\ t^{(k+1)^t}_{\mathrm{G},2} N^I_{,2} \\ t^{(k+1)^t}_{\mathrm{G},1} N^I_{,2} + t^{(k+1)^t}_{\mathrm{G},2} N^I_{,1} \end{bmatrix}, \qquad
\boldsymbol{B}^I_{\mathrm{br}} = \begin{bmatrix} N^I_{,1}\boldsymbol{\varphi}^{(k+1)}_{\mathrm{G},1} \cdot \boldsymbol{\Lambda}_I \\ N^I_{,2}\boldsymbol{\varphi}^{(k+1)}_{\mathrm{G},2} \cdot \boldsymbol{\Lambda}_I \\ N^I_{,1}\boldsymbol{\varphi}^{(k+1)}_{\mathrm{G},2} \cdot \boldsymbol{\Lambda}_I + N^I_{,2}\boldsymbol{\varphi}^{(k+1)}_{\mathrm{G},1} \cdot \boldsymbol{\Lambda}_I \end{bmatrix},
$$

$$
\boldsymbol{B}^I_{\mathrm{b}} = [\boldsymbol{B}^I_{\mathrm{bd}} \mid \boldsymbol{B}^I_{\mathrm{br}}] .
$$

(iii) **Bending strains.**

$$
\boldsymbol{\kappa}^{(k+1)}_{\mathrm{G}} = \begin{bmatrix} \boldsymbol{\varphi}^{(k+1)}_{\mathrm{G},1} \cdot t^{(k+1)}_{\mathrm{G},1} \\ \boldsymbol{\varphi}^{(k+1)}_{\mathrm{G},2} \cdot t^{(k+1)}_{\mathrm{G},2} \\ \boldsymbol{\varphi}^{(k+1)}_{\mathrm{G},1} \cdot t^{(k+1)}_{\mathrm{G},2} + \boldsymbol{\varphi}^{(k+1)}_{\mathrm{G},2} \cdot t^{(k+1)}_{\mathrm{G},1} \end{bmatrix}, \qquad
\boldsymbol{\chi}_{\mathrm{G}} = \boldsymbol{\kappa}^{(k+1)}_{\mathrm{G}} - \boldsymbol{\kappa}^{(0)}_{\mathrm{G}} .
$$

(iv) **Bending stresses.**

$$
\boldsymbol{m}_{\mathrm{G}} = \mathbb{C}_{\mathrm{b}}\boldsymbol{\chi}_{\mathrm{G}} .
$$

(v) **Bending contribution to tangent stiffness.**
— Material:

$$
\boldsymbol{MK}^{IJ}_{\mathrm{b}} = \boldsymbol{B}^{I^t}_{\mathrm{b}}\mathbb{C}_{\mathrm{b}}\boldsymbol{B}^J_{\mathrm{b}} .
$$

— Geometric–rotational:

$$
\boldsymbol{GK}^{IJ}_{\mathrm{b}\,1} = \boldsymbol{m}_{\mathrm{G}} \cdot \begin{bmatrix} N^I_{,1}N^J_{,1} \\ N^I_{,2}N^J_{,2} \\ N^I_{,1}N^J_{,2} + N^I_{,2}N^J_{,1} \end{bmatrix} (\boldsymbol{\Lambda}_I) .
$$

— Geometric–diagonal:

$$
\boldsymbol{GK}^{IJ}_{\mathrm{b}\,2} = \boldsymbol{m}_{\mathrm{G}} \cdot \begin{bmatrix} N^I_{,1}t^{(k+1)}_J \cdot \boldsymbol{\varphi}^{(k+1)}_{\mathrm{G},1} \\ N^I_{,2}t^{(k+1)}_J \cdot \boldsymbol{\varphi}^{(k+1)}_{\mathrm{G},2} \\ N^I_{,1}t^{(k+1)}_J \cdot \boldsymbol{\varphi}^{(k+1)}_{\mathrm{G},2} + N^I_{,2}t^{(k+1)}_J \cdot \boldsymbol{\varphi}^{(k+1)}_{\mathrm{G},1} \end{bmatrix} \delta^{IJ}\boldsymbol{1}_2 ,
$$

$$
\boldsymbol{K}^{IJ}_{\mathrm{b}} = \sum_{\mathrm{G}=1}^{\mathrm{G}-P_{\mathrm{ts}}} \left\{ \boldsymbol{MK}^{IJ}_{\mathrm{b}} + \begin{bmatrix} \boldsymbol{0}_{3\times3} & \boldsymbol{GK}^{IJ}_{\mathrm{b}\,1} \\ \boldsymbol{GK}^{JI^t}_{\mathrm{b}\,1} & \boldsymbol{GK}^{IJ}_{\mathrm{b}\,2} \end{bmatrix} \right\} \bar{j}^{0}_{\mathrm{G}}\mathcal{W}_{\mathrm{G}} .
$$

(vi) **Bending residual.**

$$
\boldsymbol{R}^I_{\mathrm{m}} = \sum_{\mathrm{G}=1}^{\mathrm{G}-P_{\mathrm{ts}}} \boldsymbol{B}^{I^t}_{\mathrm{m}}\boldsymbol{m}_{\mathrm{G}}\bar{j}^{0}_{\mathrm{G}}\mathcal{W}_{\mathrm{G}} .
$$

References

[1] J.C. Simo and D.D. Fox, On a stress resultant geometrically exact shell model. Part I: Formulation and optimal parametrization, Comput. Methods Appl. Mech. Engrg. 72 (1989) 267–304.

[2] S. Ahmad, B.M. Irons and O.C. Zienkiewicz, Analysis of thick and thin shell structures by curved finite elements, Internat. J. Numer. Methods Engrg. 2 (1970) 419–451.

[3] E. Ramm, A plate/shell element for large deflections and rotations, in: Formulations and Algorithms in Finite Element Analysis (MIT Press, Cambridge, MA, 1977).

[4] H. Parisch, Nonlinear analysis of shells using isoparametric elements, in: T.J.R. Hughes et al., eds., Nonlinear Finite Element Analysis of Plates and Shells (ASME, New York, 1981) 47–63.

[5] T.J.R. Hughes and W.K. Liu, Nonlinear finite element analysis of shells: Part I. Three-dimensional shells, Comput. Methods Appl. Mech. Engrg. 26 (1981) 331–362.

[6] T.J.R. Hughes and W.K. Liu, Nonlinear finite element analysis of shells — Part II. Two-dimensional shells, Comput. Methods Appl. Mech. Engrg. 27 (1981) 167–182.

[7] G. Stanley, Continuum-based shell elements, PhD dissertation, Applied Mechanics Division, Stanford University, 1985.

[8] K.K. Liu, D. Lam, S.E. Law and T. Belytschko, Resultant stress degenerated shell element, Comput. Methods Appl. Mech. Engrg. 55 (1986) 259–300.

[9] W.T. Koiter, On the nonlinear theory of thin elastic shells, Proc. Koninkl. Ned. Akad. Wetenschap., Ser B 69 (1966) 1–54.

[10] W.T. Koiter, On the foundations of the linear theory of thin elastic shells, I and II, Proc. Koninkl. Ned. Akad. Wetenschap., Ser. B 73 (1970) 169–195.

[11] E. Reissner, Linear and nonlinear theories of shells, in: Y.C. Fung and E.E. Sechler, eds., Thin-shell Structures, Sechler Anniversary Volume (Prentice Hall, New York, 1974) 29–44.

[12] E. Reissner, A note on two-dimensional finite-deformation theories of shells, Internat. J. Non-Linear Mech. 17 (3) (1982) 217–221.

[13] S.S. Antman, Ordinary differential equations of nonlinear elasticity I: Foundations of the theories of non-linearly elastic rods and shell, Arch. Rational Mech. Anal. 61 (4) (1976) 307–351.

[14] S.S. Antman, Ordinary differential equations of nonlinear elasticity II: Existency and regularity theory for conservative boundary value problems, Arch. Rational Mech. Anal. 61 (2) (1976) 353–393.

[15] J.C. Simo, J.E. Marsden and P.S. Krishnaprasad, The Hamiltonian structure of elasticity. The convective representation of solids, rods and plates, Arch. Rational Mech. Anal. 104 (2) (1988) 125–183.

[16] J.C. Simo and L. Vu-Quoc, A 3-dimensional finite strain rod model. Part II: Geometric and computational aspects, Comput. Methods Appl. Mech. Engrg. 58 (1986) 79–116.

[17] J.C. Simo and L. Vu-Quoc, A beam model including shear and torsional warping distorsions based on an exact geometric description of nonlinear deformations, Internat. J. Solids Structures (1987), to appear.

[18] J.C. Simo and L. Vu-Quoc, On the dynamics of finite-strain rods undergoing large motions—A geometrically exact approach, Comput. Methods Appl. Mech. Engrg. 66 (1988) 125–161.

[19] J.C. Simo, D.D. Fox and M.S. Rifai, On a stress resultant geometrically exact shell model, Part II: The linear theory; Computational Aspects, Comput. Methods Appl. Mech. Engrg. 73 (1989) 53–92.

[20] J.C. Simo and R.L. Taylor, Consistent tangent operators for elastoplasticity, Comput. Methods Appl. Mech. Engrg. 48 (1985) 101–118.

[21] H.B. Keller, Numerical solution of bifurcation and nonlinear eigenvalue problems, in: P. Rabinowitz, ed., Applications of Bifurcation Theory (Academic Press, New York, 1977) 359–384.

[22] W. Klingenberg, A Course in Differential Geometry, Graduate Text in Mathematics (Springer, Berlin 1978).

[23] J.C. Simo and T.J.R. Hughes, On the variational foundations of assumed strain methods, J. Appl. Mech. 53 (1) (1986) 51–54.

[24] M. Bernadou, P.G. Ciarlet and H. Jianwei, On the convergence of the semi-discrete incremental method in nonlinear, three-dimensional elasticity, J. Elasticity 14 (1984) 425–440.

[25] O.C. Zienkiewicz, The Finite Element Method (McGraw-Hill, New York, 1978).

[26] K.J. Bathe, Finite Element Procedures in Engineering Analysis (Prentice-Hall, Englewood Cliffs, NJ, 1982).

[27] T.J.R. Hughes, The Finite Element Method (Prentice-Hall, Englewood Cliffs, NJ, 1987).

[28] K.C. Park and G.M. Stanley, A curved C^0 shell element based on assumed natural-coordinate strains, J. Appl. Mech. 53 (2) (1986) 278–290.

[29] T.J.R. Hughes and M. Cohen, The 'heterosis' finite element for plate bending, Comput. & Structures 9 (1979) 445–450.

[30] P. Wriggers and J.C. Simo, A general purpose algorithm for extended systems in continuation methods, Internat. J. Numer. Methods Engrg., to appear.

[31] J.H. Argyris, H. Balmer, J.St. Doltsinis, P.C. Dunne, M. Haase, M. Hasse, M. Kleiber, G.A. Malejannakis, H.P. Mlejenek, M. Muller and D.W. Scharpf, Finite element method—The natural approach, Comput. Methods Appl. Mech. Engrg. 17/18 (1979) 1–106.

[32] J.C. Simo, P. Wriggers, K.H. Schweizerhoff and R.L. Taylor, Post-buckling analysis involving inelasticity and unilateral constraints, Internat. J. Numer. Methods Engrg. 23 (1986) 779–800.

[33] D. Bushnell, Computerized Buckling Analysis of Shells, Mechanics of Elastic Stability, Vol. 9 (Martinus Nijhoff, Boston, 1985).

[34] S.P. Timoshenko and J.M. Gere, Theory of Elastic Stability (McGraw-Hill, New York, 1961).

[35] N.J. Hoff and T.C. Soong, Buckling of circular cylindrical shells in axial compression, Internat. J. Mech. Sci. 7 (1965) 489–520.

[36] W.C. Rheinboldt, Methods for solving systems of nonlinear equations, CBMS Regional Conference Series in Applied Mathematics 14, Society for Industrial and Applied Mathematics, Philadelphia, 1974.

[37] W.C. Rheinboldt, Numerical Analysis of Parametrized Nonlinear Equations (Wiley/Interscience, New York, 1986).

[38] K.H. Schweizerhof and P. Wriggers, Consistent linearization of path following methods in nonlinear FE analysis, Comput. Methods Appl. Mech. Engrg. 59 (1986) 261–279.

[39] G. Horrigmoe, Finite element instability analysis of free-form shells, Report 77–2, Division of Structural Mechanics, Norwegian Institute of Technology, University of Trondheim, Norway, 1977.

[40] P.G. Bergan, G. Horrigmoe, B. Krakeland and T.H. Soreide, Solution techniques for nonlinear finite element problems, Internat. J. Numer. Methods Engrg. 12 (1978) 1677–1696.

[41] P. Wriggers, P. Wagner and C. Miehe, A quadratic convergent procedure for the calculation of stability points in finite element analysis, Comput. Methods Appl. Mech. Engrg. 70 (1988) 329–347.

[42] L.A. Taber, Large deflection of a fluid-filled spherical shell under a point load, J. Appl. Mech. 49 (1982) 121–128.

[43] L.H. Donnell and C.C. Wan, Effect of imperfections on buckling of thin cylinders and columns under axial compression, J. Appl. Mech. 17 (1950) 73–83.

[44] C. Steele (1989) Private communication.